Research Square

Preprints are preliminary reports that have not undergone peer review.
They should not be considered conclusive, used to inform clinical practice,
or referenced by the media as validated information.

Effects of joint roughness on roadway deformation, damage and rockbolt response under different lateral pressure coefficients

Haoyu Sun
University of Science and Technology Beijing
Peitao Wang
wangpeitao@ustb.edu.cn
University of Science and Technology Beijing
Qi Gou
University of Science and Technology Beijing
Yi Chai
Anhui Magang Luohe Mining Industry Co., Ltd
Long Tao
Anhui Magang Luohe Mining Industry Co., Ltd

Research Article

Keywords: Joint roughness, Discrete fracture network, Lateral pressure coefficient, Rockbolt support, Damage evolution

Posted Date: November 23rd, 2026

DOI: https://doi.org/10.21203/rs.3.rs-11706265/v1

License: This work is licensed under a Creative Commons Attribution 4.0 International License.
Read Full License

Additional Declarations: No competing interests reported.

Effects of joint roughness on roadway deformation, damage and rockbolt response under different lateral pressure coefficients

Haoyu Sun [1,3], Peitao Wang [1,3*], Qi Gou [1,3], Yi Chai [2], Long Tao [2]

1. China-Zambia Belt and Road Joint Laboratory on Green and Safe Development of Mineral Resources, University of Science and Technology Beijing, Beijing 100083, China

2. Anhui Magang Luohe Mining Industry Co., Ltd., Hefei 231500, China

3. Key Laboratory of Ministry of Education for Efficient Mining and Safety of Metal Mine, University of Science and Technology Beijing, Beijing 100083, China

*** Corresponding author:** Peitao Wang

E-mail: wangpeitao@ustb.edu.cn

Highlights:

- Higher lateral stress reverses maximum displacement rankings in unsupported models.
- Reported bond-breakage counts were lower in the supported models.
- At K = 1.87, the local mean particle force at the middle segment of bolt 1-1 dropped later in the RDFN than in the DFN.

Abstract: Excavation redistributes stresses in jointed rock around underground mine roadways, leading to deformation and damage. How lateral stress modifies the effects of joint roughness on roadway deformation, damage and rockbolt response remains unclear. Based on field joint surveys at the Shilu Iron Mine and laboratory-calibrated parameters, paired three-dimensional Particle Flow Code (PFC) models were developed with rough and planar discrete fracture networks (RDFN and DFN, respectively). The models shared fracture arrangements and mechanical parameters, with rough surfaces generated using the Weierstrass–Mandelbrot function. Simulations were conducted with and without rockbolt support at initial lateral pressure coefficients (K) of 1.0 and 1.87. At cycle 40,000, increasing K from 1.0 to 1.87 raised the maximum displacement from 0.1230 to 0.2050 m in the unsupported RDFN and from 0.0950 to 0.2436 m in the unsupported DFN. At K = 1.87, the reported cumulative bond-breakage counts were 9,810 and 6,179 for the supported RDFN and DFN, compared with 19,833 and 14,443 for their unsupported counterparts. At the same K, the local mean particle force at the middle segment of horizontal bolt 1-1 dropped abruptly after its peak, with the drop occurring later in the RDFN. Relative to the rough-joint model, planar-joint idealisation underestimated maximum displacement at K = 1.0 and overestimated it at K = 1.87. These findings provide a basis for selecting joint representations and interpreting deformation, damage and rockbolt response in numerical assessments of mine roadway support.

Keywords: Joint roughness; Discrete fracture network; Lateral pressure coefficient; Rockbolt support; Damage evolution;

1 Introduction

Stable underground roadways are essential for safe access and production in metal mines, particularly as mining extends to greater depths (Cai et al. 2019). Excavation redistributes the in situ stresses around a roadway, and the resulting deformation and damage depend on the structure of the rock mass and the restraint provided by the support. Studies of deep fractured rock and highly stressed soft rock have shown how deterioration of the surrounding rock can undermine the structures that carry load around an opening (Li et al. 2015; SR Zhang et al. 2025). In jointed hard-rock roadways, the resulting demand on rockbolts depends on how the joint network deforms under the prevailing stress conditions.

Experiments and numerical studies show that joint spacing, orientation and connectivity influence rock fragmentation and crack propagation around excavations (Chen et al. 2017; Yang et al. 2019; Chen et al. 2020; M Li et al. 2024). Joint orientation also affects the sensitivity of the rock adjacent to an opening to joint micromechanical parameters (Yang and Kulatilake 2019). Combining photogrammetry with discrete fracture network (DFN) modelling allows mapped discontinuities to inform excavation analyses (Sarmast Sakhvidi et al. 2026). The mechanical response can still differ between networks with similar geometric statistics (Yin and Chen 2020). Studies of lined openings, fault-crossing roadways and layered tunnels further show that the structure of the surrounding rock influences how reinforcement controls deformation and damage (Fan et al. 2021; HB Li et al. 2024; Zhang et al. 2026). These findings establish the need to consider joint geometry when evaluating support response.

Joint surface morphology affects shear resistance and crack development. The contribution of roughness to shear strength varies with scale, and fractal descriptions of natural joints require information on both geometric complexity and surface relief (Barton 1973; Bandis et al. 1981; Kulatilake et al. 2006). Numerical studies of rough fracture networks have documented changes in stiffness, peak strength and failure patterns under compression and direct shear (Wang et al. 2017; Wang et al. 2018; Wang et al. 2020). The Weierstrass-Mandelbrot function has extended this

approach to three-dimensional rough discrete fracture network (RDFN) (Wang et al. 2023b). Applications to specimens with openings and to jointed rock under compression show that roughness acts alongside opening geometry, joint inclination and bond strength in shaping the mechanical response (Wang et al. 2023a; Gou et al. 2024).

The effects of joint geometry also depend on loading. At the joint scale, higher normal stress and greater roughness can promote localised bond breakage, while stress perturbations can trigger slip along discontinuities close to failure (Meng et al. 2022; Hu et al. 2026). True triaxial studies have linked crack initiation to joint asperities and shown that the effect of lateral stress on the shear strength of intermittent joints can be nonmonotonic (Xue et al. 2026; Zheng et al. 2025). Studies of layered rock likewise indicate that interface properties and the unloading path influence whether fractures follow or cross bedding (Wang et al. 2026; Liu et al. 2026). These studies describe local failure processes that can contribute to the response of a jointed rock mass around a roadway.

At the roadway scale, it remains unclear whether rough and planar networks retain the same ordering of maximum displacement as lateral stress changes. A reversal would mean that a planar network could give either a lower or a higher displacement estimate than its rough counterpart, depending on lateral stress. Isolating the effect of surface morphology requires paired networks that share joint locations, orientations and sizes, with their responses compared under the same loading conditions.

A related question is how rockbolting changes the contrasts between rough and planar networks. A comparison based on maximum displacement characterises deformation control and leaves open whether the networks also give comparable cumulative bond-breakage counts or similar force histories at monitored bolt locations. Paired comparisons with and without rockbolts are therefore needed to examine how deformation control, damage accumulation and local bolt response vary with joint morphology and lateral stress. Each comparison must account for the output stage used for the corresponding indicator.

This study uses photogrammetric joint surveys from the −360 m mining level of the Shilu Iron Mine and parameters calibrated against laboratory uniaxial compression tests to build paired three-dimensional roadway models in the Particle Flow Code (PFC). The rough and planar networks share their fracture arrangement and mechanical parameters. Eight simulations combine the two networks, two initial lateral pressure coefficients (K = 1.0 and 1.87) and two support conditions. The analysis compares roadway displacement, cumulative bond-breakage counts, surrounding-rock stress and local mean particle forces at representative bolt locations. The displacement results reveal a reversal in the maximum-displacement ordering of the unsupported models. The crack outputs describe spatial patterns and cumulative bond breakage in each case. The bolt-force histories identify a later post-peak force drop in the rough model at the middle segment of the monitored horizontal bolt. These results inform the use of planar-joint idealisation and the interpretation of rockbolt support performance under the modelled stress conditions.

2 Numerical model development and simulation scheme

2.1 Joint geometry characterisation and fracture network generation

Joint surveys were conducted at survey station 9 at the -360 m level of the Shilu Iron Mine using the SIROVISION digital photogrammetry system. Paired images were processed to reconstruct the exposed rock surface in three dimensions, from which joint dip direction, dip angle, trace length and spacing were characterised. The dataset contains 283 joint records assigned to three dominant sets, comprising 73, 127 and 83 records, respectively. Table 1 presents the geometry statistics adopted for network generation. Its trace-length statistics are processed model inputs: for sets 1-3, the recorded traces were increased by 0.40, 0.30 and 0.40 m, respectively, giving mean input lengths of 0.487, 0.393 and 0.508 m. These values therefore differ from the means of the unadjusted recorded traces, approximately 0.087, 0.093 and 0.108 m.

The survey data were fitted with probability distributions. Trace lengths were described by lognormal distributions for all three sets; dip angles were described by exponential distributions for

sets 1 and 3 and a uniform distribution for set 2. The reported dip-direction fits were normal for set 1 and lognormal for set 2. These distribution summaries describe the processed survey data. Statistical agreement between fracture networks does not necessarily imply mechanical equivalence. The scaling of fracture populations, three-dimensional network generation and representative-volume assessment provide complementary foundations for network modelling (Bonnet et al. 2001; Huang et al. 2021). Here, one common spatial realisation was retained for the morphology comparison; variability among alternative networks was not evaluated.

Table 1 Statistical characteristics of joint geometry measured in the field

Joint set	Statistic	Dip direction (°)	Dip angle (°)	Trace length (m)	Spacing (m)	Linear intensity (m^{-1})
1	Mean	186.8	69.7	0.487	0.247	4.046
	Standard deviation	22.3	14.3	0.046	0.224	
2	Mean	282.2	28.3	0.393	0.167	5.988
	Standard deviation	55.8	22.5	0.066	0.037	
3	Mean	21.3	67.8	0.508	0.199	5.023
	Standard deviation	24.3	14.4	0.081	0.080	

The adopted geometry statistics and linear fracture intensity were used to construct the DFN in MATLAB within a Monte Carlo network-generation framework. Rough joint surfaces with stochastic undulations were then generated using the W-M fractal function to construct the RDFN (Komvopoulos and Ye 2001; Cui et al. 2022). The adopted three-dimensional RDFN framework links W-M surface parameters to roughness and incorporates the resulting networks into particle-based models (Wang et al. 2023b). The joint surface profile height is expressed as

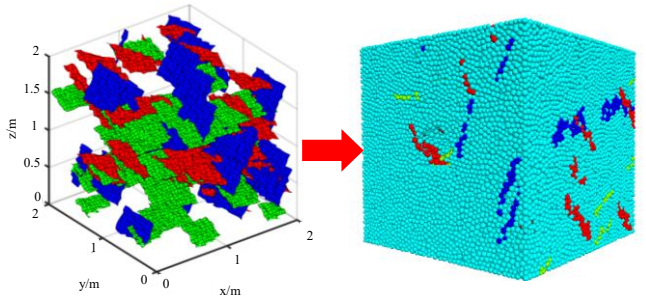
$$z(x,y) = L\left(\frac{G}{L}\right)^{D-2}\left(\frac{\ln\gamma}{M}\right)\sum_{n=0}^{n_{\max}}\gamma^{n(D-3)}\left\{\cos\varphi_{m,n} - \cos\left[\frac{2\pi\gamma^{n}\left(x^{2}+y^{2}\right)^{\frac{1}{2}}}{L}\bullet\cos\left(\tan^{-1}\left(\frac{y}{x}\right)-\frac{\pi m}{M}+\varphi_{m,n}\right)\right]\right\} \quad (1)$$

where $z(x, y)$ is the profile height of the three-dimensional random rough surface; x and y are spatial coordinates; L is the sampling length used to scale the surface in each direction; G is the fractal height amplitude, also termed the characteristic scale parameter; and D is the fractal dimension ($2 < D < 3$). The parameters G and D primarily control the W-M surface profile. The spatial frequency density factor γ ($\gamma > 1$) controls the frequency distribution; M is the number of superimposed asperities on the surface; n is the frequency index, with an upper limit of $n_{\max}$; and $\varphi_{m,n}$ is a prescribed or variable random phase that determines whether the generated surface is fixed or random.

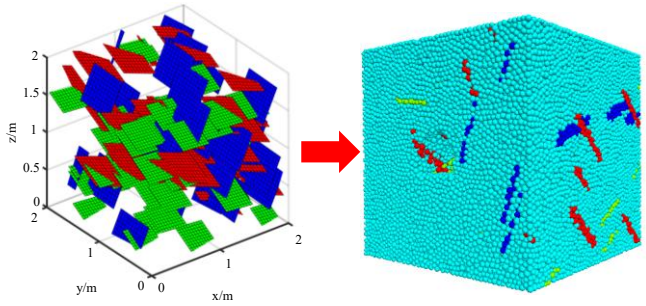
The adopted roughness parameters were $D = 2.52$, $G = 10^{-6.2}$ and $P = 10$. Here, P is the ratio of the surface sampling length to the discretization step; $P = 10$ divides the sampled surface into a 10 × 10 grid. These parameter values were selected based on comparisons between fractal-generated profiles and joint roughness profiles, together with preliminary sensitivity analyses of single-joint models. Those analyses distinguished the effects of D and G on surface relief from the influence of P on discretization and stiffness. The adopted values represent one roughness configuration, rather than a measured roughness distribution or a roadway-scale convergence study. The DFN and RDFN had the same joint centres, orientations, overall sizes and numbers; only surface morphology differed (Fig. 1).

Quantitative profile descriptors provide complementary approaches to roughness calibration. Measurements of natural sandstone fractures show that surface roughness varies with observation scale and exhibits self-affine behaviour (Houben et al. 2024). A two-dimensional geometric parameter has been related to the joint roughness coefficient (JRC) (Tatone and Grasselli 2010). Profile-length ratio and maximum undulation have also been incorporated into JRC estimation, while estimates combining relief amplitude and gradient are sensitive to the sampling interval (Tang et al.

2021; Yuan et al. 2021). These approaches were not applied in this study; therefore, the adopted parameters should not be interpreted as a site-calibrated JRC distribution.



(a) RDFN model



(b) DFN model

Fig. 1 RDFN and DFN fracture networks and particle models

2.2 Calibration and determination of joint parameters

The macroscopic response of a particle-based discrete element model implemented in Particle Flow Code (PFC) is governed jointly by micromechanical parameters such as contact stiffness, bond strength and friction. The linear parallel bond model was used to describe force and moment transmission and bond failure between particles representing intact rock. Particle stiffness, parallel bond stiffness, bond strengths and friction parameters were adjusted to reproduce the elastic modulus, uniaxial compressive strength and failure mode measured in laboratory tests.

The calibration results are shown in Fig. 2. The numerical specimen had an elastic modulus of 70.16 GPa and a uniaxial compressive strength of 79.52 MPa, compared with laboratory values of 77.02 GPa and 80.13 MPa, respectively. The corresponding relative errors were 8.91% and 0.76%. Post-peak cracks propagated predominantly in the axial direction, accompanied by localised inclined cracks, consistent with the macroscopic failure characteristics of the laboratory specimen.

Calibration does not eliminate uncertainty associated with particle and joint representation. A bonded-particle study identified a particle-size dependence of mode-I fracture toughness and developed a coarse-graining correction for tensile strength. These findings highlight the need to assess tensile response and particle-size sensitivity in addition to matching uniaxial compressive properties (Shang et al. 2024). Earlier clumped-particle modelling also illustrates that particle representation can affect simulated rock behaviour (Cho et al. 2007). Accordingly, the present intact-rock calibration alone does not validate jointed-rock behaviour under all stress paths.

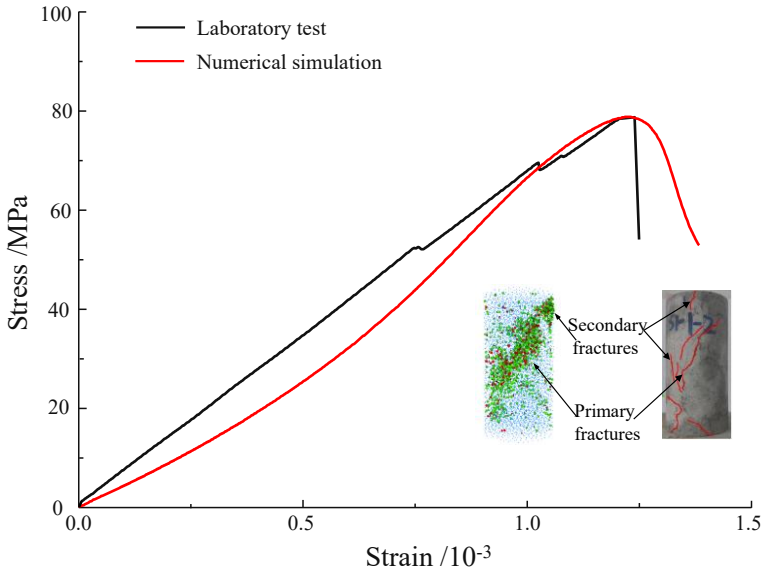


Fig. 2 Comparison of uniaxial compression calibration results and failure modes

The micromechanical parameters of intact rock and joints are listed in Table 2. Previous numerical tests indicated that joint bond strengths equal to 3%-9% of those of intact rock reproduced laboratory failure patterns reasonably well (Wang et al. 2016). Accordingly, joint bond strengths were set to 5% of the corresponding intact-rock values, while the remaining stiffness and friction parameters were unchanged. Identical mechanical parameters were assigned to the DFN and RDFN; only joint surface morphology differed.

Table 2 Micromechanical parameters of the jointed rock mass model

Micromechanical parameter	Symbol or PFC keyword	Value	Model component
Particle radius ratio	R_{max}/R_{min}	1.5	Particle assembly
Particle density (kg/m³)	density	2500	Particle assembly
Particle friction coefficient	fric	0.58	Particle assembly
Linear effective modulus (Pa)	emod	1×10^9	Linear parallel bond
Linear normal-to-shear stiffness ratio	kratio	1.0	Linear parallel bond
Parallel bond effective modulus (Pa)	pb_emod	9.36×10^{11}	Linear parallel bond
Parallel bond normal-to-shear stiffness ratio	pb_kratio	1.66	Linear parallel bond
Parallel bond cohesion (Pa)	pb_coh	1.2×10^8	Linear parallel bond
Parallel bond tensile strength (Pa)	pb_ten	3×10^7	Linear parallel bond
Joint parallel bond cohesion (Pa)	pb_coh	6×10^6	Linear parallel bond
Joint parallel bond tensile strength (Pa)	pb_ten	1.5×10^6	Linear parallel bond
Parallel bond friction angle (°)	pb_fa	45	Linear parallel bond
Friction coefficient	fric	0.58	Linear parallel bond

2.3 Roadway model and rockbolt support

A three-dimensional particle assembly measuring 2 m × 2 m × 2 m was used to balance fracture-network resolution and computational cost. The geometry was reduced by a factor of ten relative to a 20 m × 20 m × 20 m field region: the 4.5 m wide and 3.8 m high roadway corresponded to a horseshoe-shaped opening 0.45 m wide and 0.38 m high. The modelled grouted bolts were 0.30 m long, with a nominal diameter of 14 mm, an in-row spacing of 0.12 m and a row spacing of 0.25 m. Seven bolts were arranged around the upper half of the perimeter in each of six rows.

The geometric reduction does not constitute a complete mechanical similitude scheme. The model retained calibrated material parameters and the prescribed stress levels, and gravitational acceleration was not scaled. Bolt dimensions are reported as numerical inputs; a separate similitude relationship for the bolt diameter was not established. No displacement or force scaling factor was applied to the reported results: displacements and bolt forces are numerical-model quantities, not back-calculated field predictions. The comparisons therefore concern relative responses under a common modelling framework. Quantitative extrapolation to field convergence or bolt capacity requires further validation of the scaling relationships.

The fracture networks were embedded in the particle assembly, and particles within the roadway profile were removed to form the opening. For supported models, particles occupying the intended bolt holes were also removed before bolt particles were generated, avoiding excessive initial overlap. Bolt particle centres were prescribed between the exposed and embedded ends, and the resulting bolt arrangement was repeated at the specified longitudinal spacing. Bonded particle chains represented the bolt bodies; separate contact groups represented bolt-rock and bolt-joint interactions (Fig. 3; Table 3). Higher bond stiffnesses and strengths were assigned to bolt bodies than to their interfaces. Unsupported and supported assemblies were prepared as separate cases, rather than as a simulation of progressive field bolt installation. The contact parameters represent an equivalent anchorage response; the interfaces were not independently calibrated against bond-slip or pull-out data.

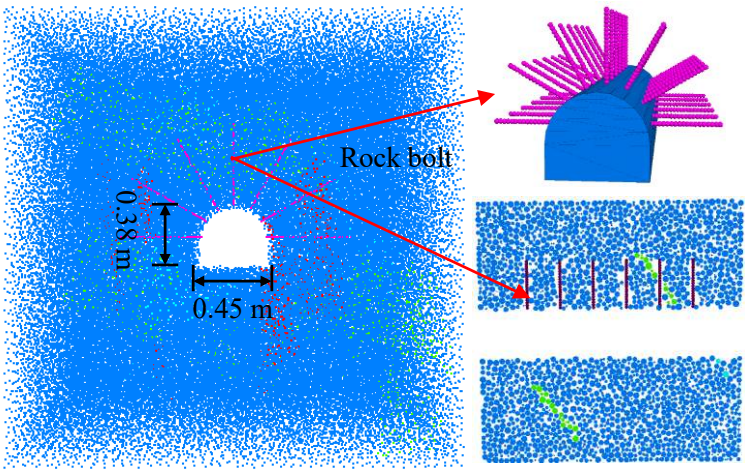


Fig. 3 Rockbolt layout and numerical representation

Table 3 Micromechanical parameters of the rockbolts and their interfaces

Component	pb_emod (Pa)	pb_kratio	pb_coh (Pa)	pb_ten (Pa)	pb_fa (°)	fric
Bolt body	1.5×10^{12}	1.66	3×10^{8}	6×10^{7}	45	0.58
Bolt–rock interface	9.36×10^{11}	1.66	2.1×10^{8}	5×10^{7}	45	0.5
Bolt–joint interface	9.36×10^{11}	1.66	1.5×10^{8}	3×10^{7}	45	0.5

2.4 Simulation scheme and response monitoring

The initial model stress state was prescribed to represent gravitational and horizontal tectonic stresses. Following preloading to reduce unbalanced forces, gravity was applied without scaling its acceleration, and biaxial boundary servo control was used to establish the prescribed horizontal and vertical stresses. The initial vertical stress was set to 19.17 MPa based on the estimated overburden weight at the -360 m mining level. The lateral pressure coefficient is defined as

$$K = \frac{\sigma_h}{\sigma_v} \tag{2}$$

where σ_h and σ_v denote the prescribed horizontal and vertical stresses during initialisation. With $\sigma_v = 19.17$ MPa, $K = 1.0$ and 1.87 correspond to $\sigma_h = 19.17$ and approximately 35.85 MPa, respectively. The former provides a reference state with equal horizontal and vertical stresses; the latter was selected from the lateral pressure coefficient reported by the preceding site measurements. These two values specify the biaxial comparison, rather than a complete measured three-dimensional stress tensor.

Each stress ratio was combined with RDFN or DFN geometry and an unsupported or supported assembly, resulting in eight simulation cases (Table 4). The numerical sequence comprised preloading to reduce excessive unbalanced forces, application of self-weight, and biaxial boundary servo control to establish the target horizontal and vertical loading. The Z axis is vertical, and its servo control was deactivated during the subsequent response calculation. K therefore characterises initialisation and is not assumed to remain constant during redistribution. All cases used the same

preparation and calculation sequence. Deactivation of servo control alone does not establish a constant-stress or traction-free boundary condition; interpretation is restricted to the adopted numerical protocol.

Table 4 Numerical simulation cases

Case	Fracture network	Lateral pressure coefficient K	Support condition
1	DFN	1.00	Unsupported
2	RDFN	1.00	Unsupported
3	DFN	1.00	Rockbolt-supported
4	RDFN	1.00	Rockbolt-supported
5	DFN	1.87	Unsupported
6	RDFN	1.87	Unsupported
7	DFN	1.87	Rockbolt-supported
8	RDFN	1.87	Rockbolt-supported

Particle velocities, surrounding-rock displacements and microcracks generated by bond breakage were recorded during the simulation. Displacement monitoring points at the crown, floor and both sidewalls quantified differences in displacement response and helped delineate the zone disturbed by excavation. Measurement circles were positioned at the roof arch and both sidewalls relative to the roadway centre (Fig. 4). The stress histories from these circles tracked post-excavation stress redistribution and characterised stress concentrations near the roadway boundary. Rock mass damage was characterised by the number and spatial distribution of microcracks.

To examine load transfer along the bolts, representative horizontal and roof bolts in rows 1, 3 and 5 were monitored throughout the simulation. Monitoring locations were set at the exposed end, midsection and anchored end of each bolt (Fig. 4). At each location, contact forces recorded for neighbouring bolt particles were averaged to smooth local fluctuations. The resulting mean force

histories were used to analyse how the load was distributed along the bolts and how that distribution evolved during the simulation.

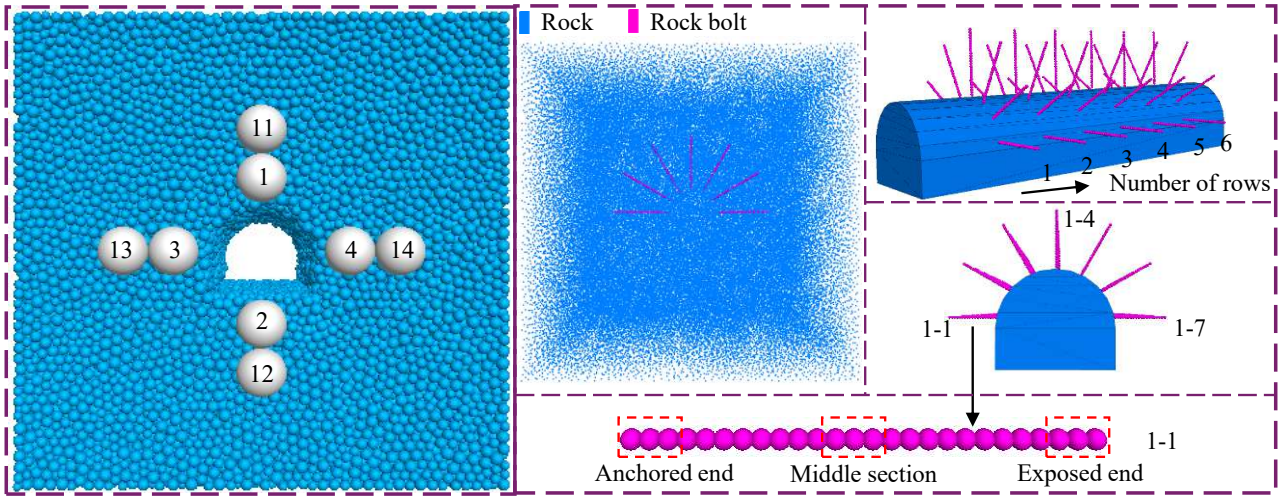


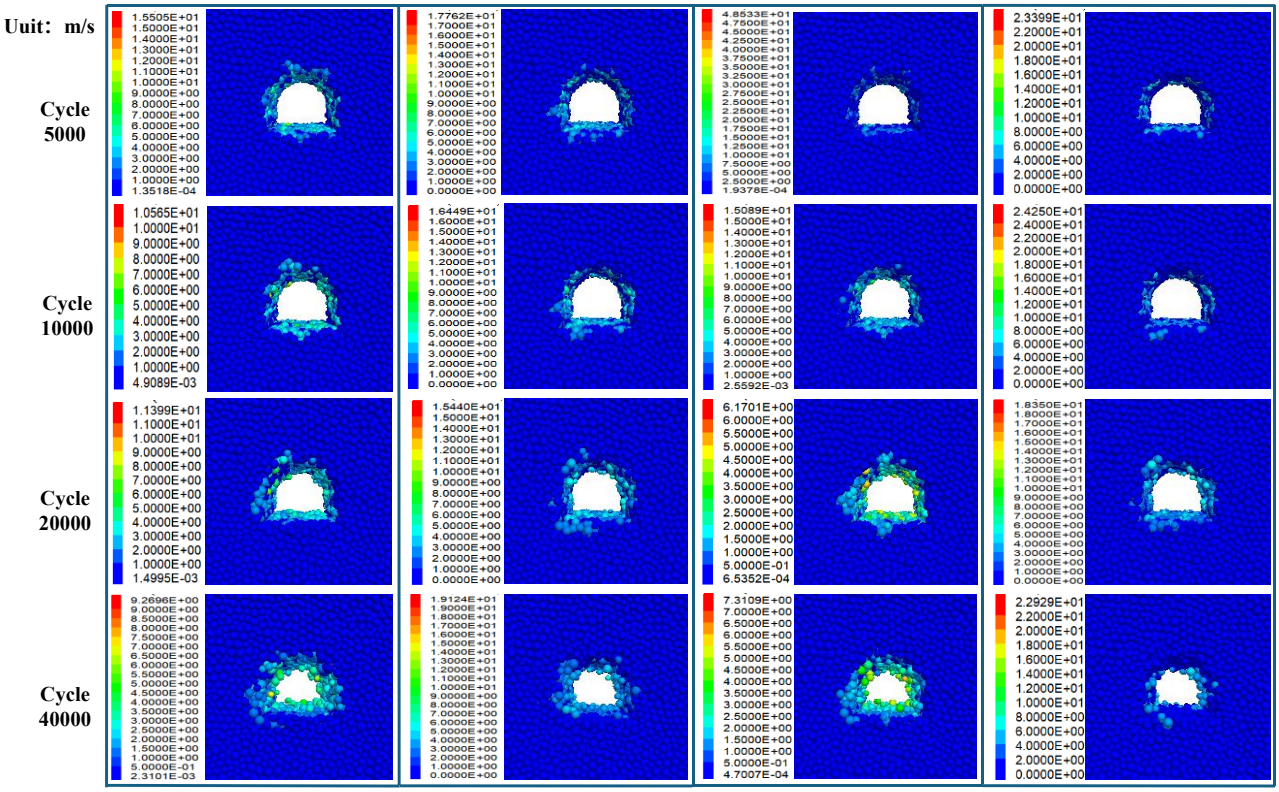
Fig. 4 Arrangement of stress and rockbolt force monitoring locations

3 Roadway deformation under different lateral stress conditions

3.1 Evolution of surrounding rock deformation

Particle velocity fields and cumulative displacement fields were extracted for the unsupported and supported RDFN and DFN models at K = 1.0 and 1.87 to investigate the spatial evolution of deformation over successive calculation stages. Particle velocity identifies actively moving regions, whereas cumulative displacement characterises accumulated model deformation. The velocity fields are numerical response indicators and have not been calibrated as field movement rates.

The particle velocity fields at K = 1.0 are shown in Fig. 5.



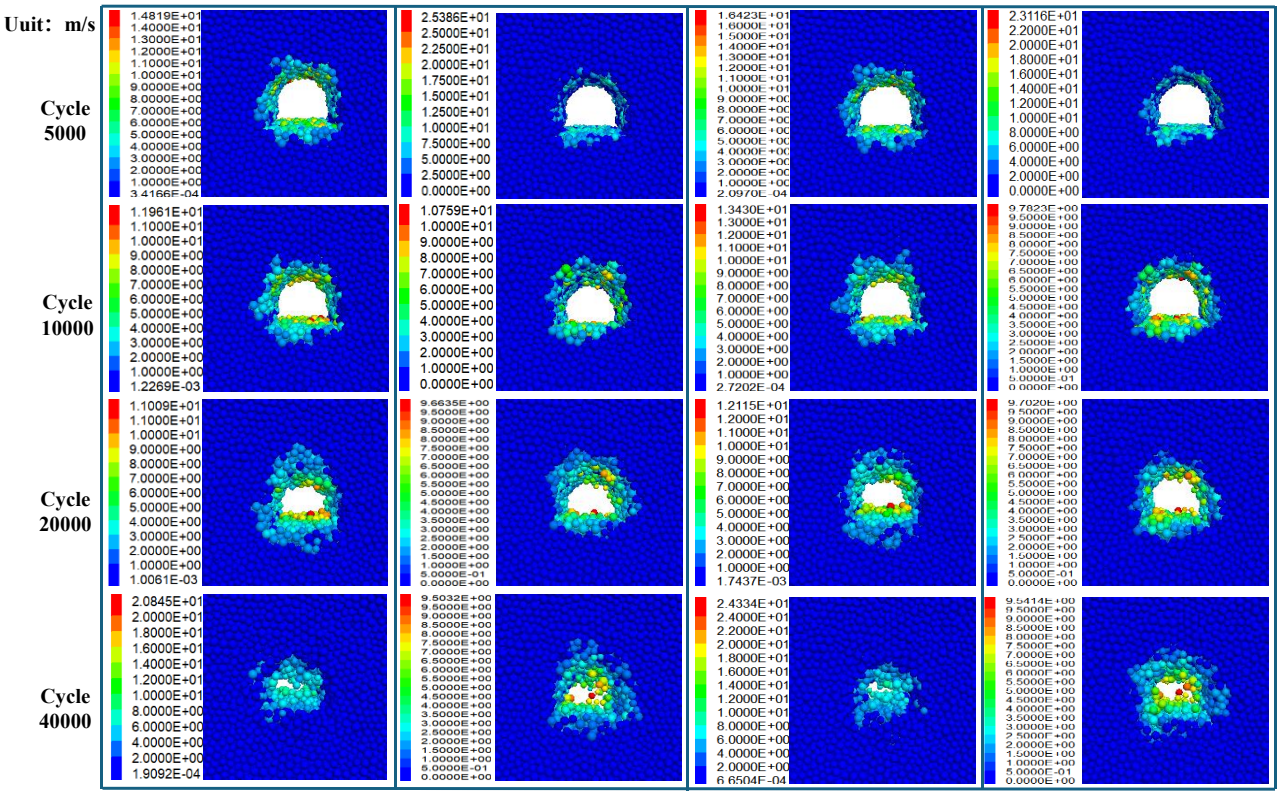
(a) RDFN-Unsupported model (b) RDFN-Support model (c) DFN-Unsupported model (d) DFN-Support model

Fig. 5 Particle velocity fields of the RDFN and DFN models at K = 1.0

Following excavation, high-velocity particles were initially concentrated near the roadway boundary and subsequently redistributed within localised regions of the roof arch, floor and sidewalls (Fig. 5). Both models exhibited pronounced localisation, but the positions and connectivity of high-velocity zones differed. During some calculation stages, the DFN developed relatively continuous zones of particle motion along the roadway perimeter, whereas high-velocity particles were more dispersed in the RDFN. Joint morphology therefore changed the spatial organisation of particle motion induced by excavation. With support, high-velocity particles remained concentrated in the near field, but their distribution changed substantially, indicating that rockbolts constrained local movement paths.

Higher lateral stress expanded the region of particle motion (Fig. 6). Active regions developed around the roof, floor and both sidewalls, indicating more spatially extensive deformation. Local velocity distributions still differed between the RDFN and DFN, but the overall extents of the active regions became similar. The contrast was therefore expressed mainly in the locations and connectivity

of localised high-velocity zones. These patterns identify where motion developed; they do not independently quantify joint sliding or energy release.



(a) RDFN-Unsupported model (b) RDFN-Support model (c) DFN-Unsupported model (d) DFN-Support model

Fig. 6 Particle velocity fields of the RDFN and DFN models at K = 1.87

Particle velocity represents only instantaneous motion at a given calculation state. Cumulative displacement was therefore examined to evaluate the extent of deformation. Fig. 7 shows the displacement distributions at different calculation cycles for K = 1.0.

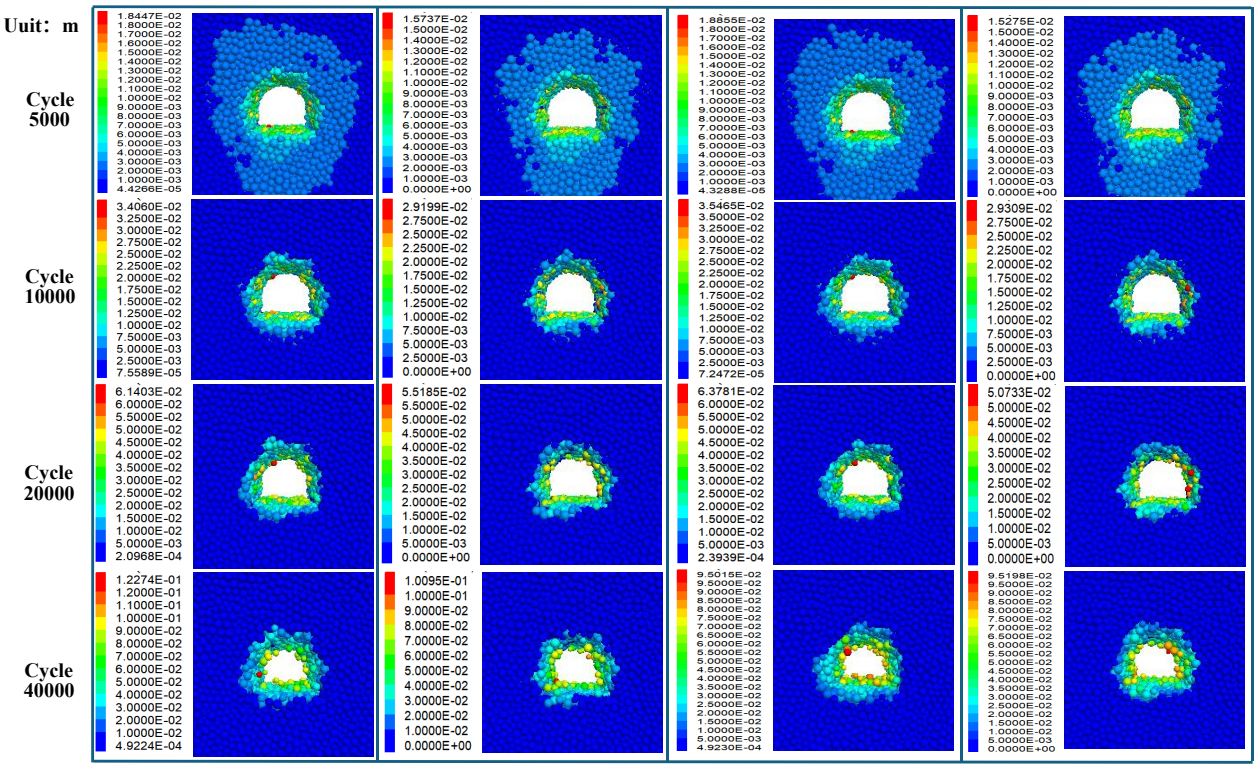


Fig. 7 Displacement distributions of the RDFN and DFN models at different calculation cycles for $K = 1.0$

As the calculation proceeded, high-displacement zones in all four models extended progressively from the roadway boundary into the surrounding rock (Fig. 7). The maximum displacement in the unsupported RDFN increased from 0.0184 m at cycle 5,000 to 0.1230 m at cycle 40,000, while that in the unsupported DFN increased from 0.0189 to 0.0950 m. Their displacement magnitudes were similar initially but diverged with continued calculation, indicating that the influence of joint morphology on cumulative deformation developed progressively. With support, the maximum RDFN displacement at cycle 40,000 was approximately 0.101 m, a reduction of about 17.8%. The supported DFN reached approximately 0.0952 m, close to its unsupported value. At K = 1.0, rockbolting therefore controlled the maximum RDFN displacement more effectively, whereas the maximum DFN displacement was relatively insensitive to support. Because peak displacement reflects a localised extreme, the extent of high-displacement zones was also examined.

At K = 1.87, cumulative displacement increased markedly in all four models (Fig. 8).

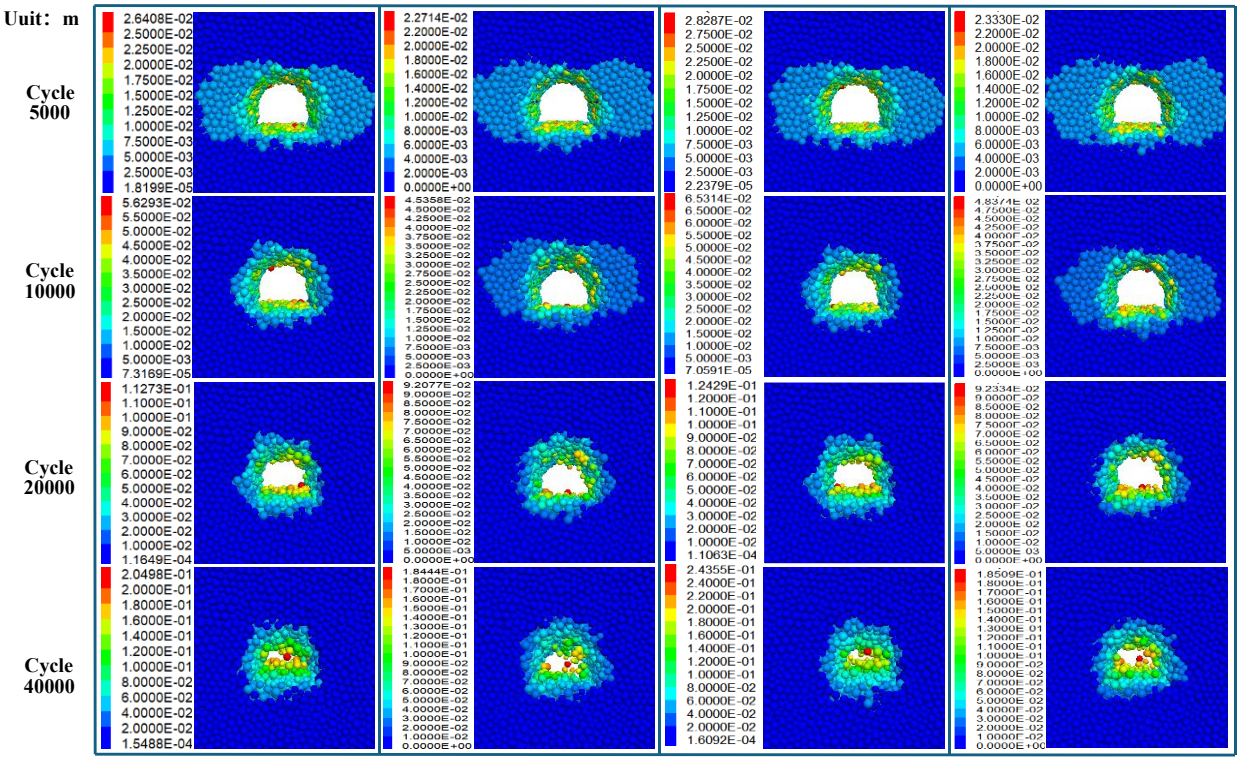


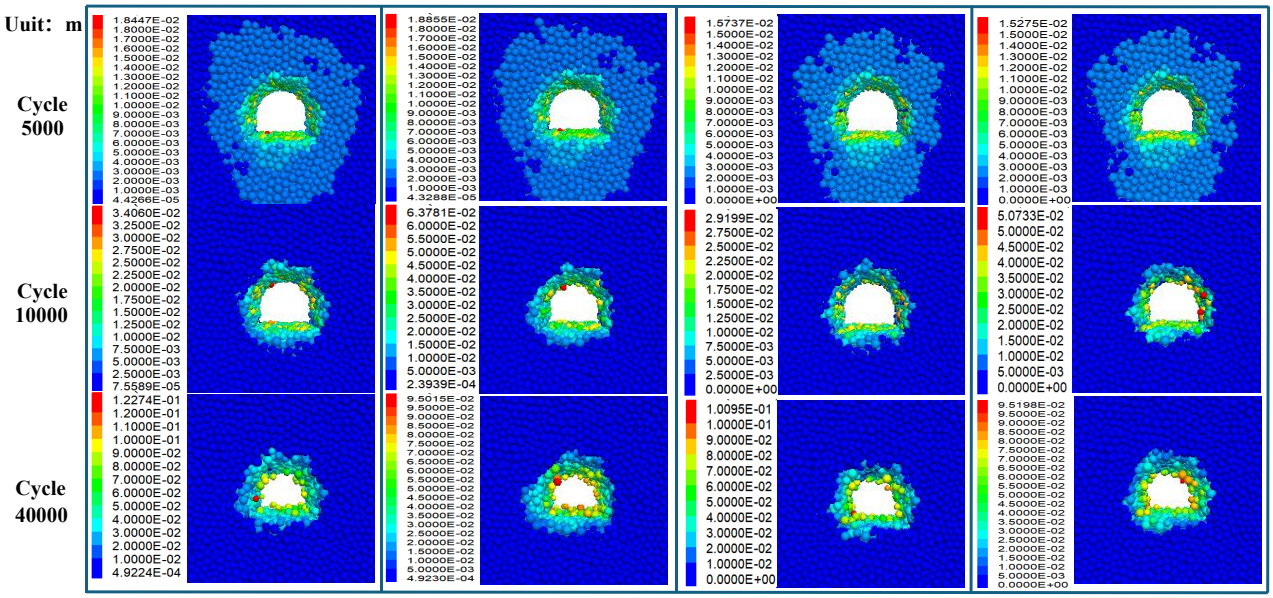
Fig. 8 Displacement distributions of the RDFN and DFN models at different calculation cycles for $K = 1.87$

At cycle 40,000, the unsupported RDFN and DFN reached maximum displacements of approximately 0.2050 and 0.2436 m, respectively, or 1.67 and 2.56 times their corresponding values at $K = 1.0$ (Fig. 8). With rockbolting, these maxima decreased to approximately 0.1844 and 0.1851 m, corresponding to reductions of 10.0% in the RDFN and 24.0% in the DFN relative to their unsupported counterparts. The absolute gap between the model maxima narrowed from approximately 0.0386 m to 0.00065 m.

3.2 Influence of the lateral pressure coefficient on deformation patterns

The comparisons below focus on where displacement is concentrated and how it extends around the opening. RDFN and DFN patterns were compared at the same lateral pressure coefficient and support condition. For each fracture network, the supported and unsupported cases were then compared at the same calculation cycle.

The comparisons at $K = 1.0$ are shown in Fig. 9.



(a) RDFN-Unsupported model (b) DFN-Unsupported model (c) RDFN-Support model (d) DFN-Support model

Fig. 9 Comparison of displacement distributions in supported and unsupported RDFN and DFN models at $K = 1.0$

At K = 1.0, the unsupported RDFN and DFN showed similar displacement patterns at cycle 5,000, but their spatial distributions diverged by cycle 40,000 (Fig. 9(a,b)). In the RDFN, the larger displacements were grouped in localised clusters adjacent to the excavation. The DFN showed a more continuous band extending from the left sidewall towards the floor. With support, this band became less continuous in the DFN, while the RDFN clusters were concentrated closer to the opening (Fig. 9(c,d)). The spatial arrangement therefore changed in the DFN even though its maximum displacement changed little.

Fig. 10 compares the displacement distributions of the RDFN and DFN at K = 1.87 under unsupported and rockbolt-supported conditions.

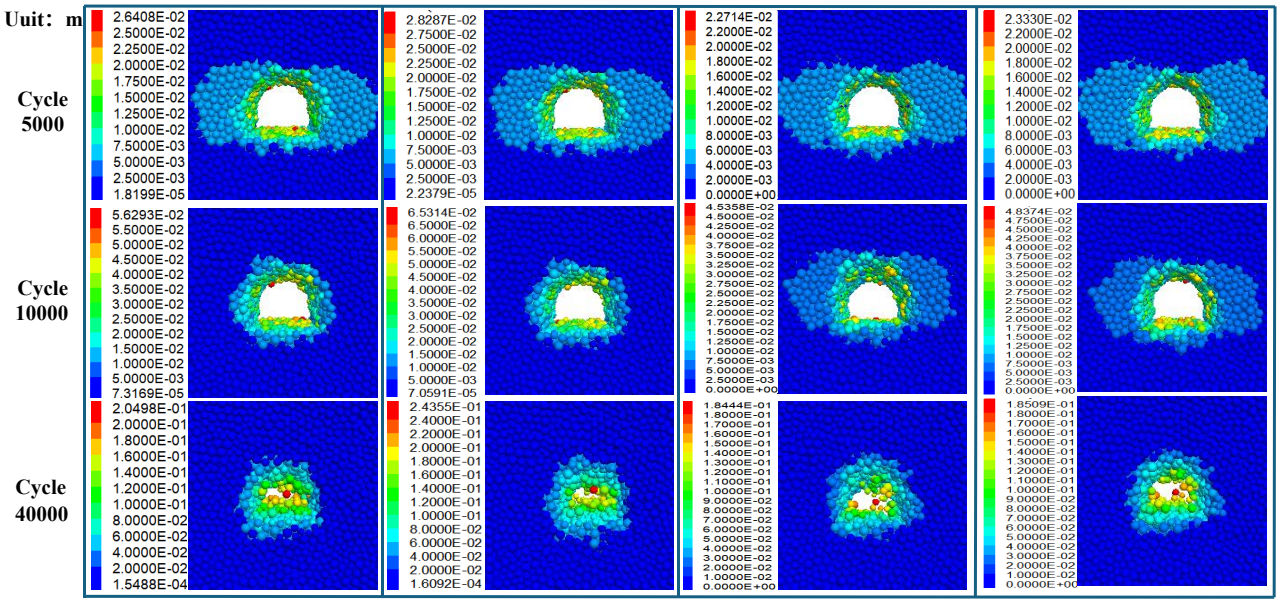


Fig. 10 Comparison of displacement distributions in supported and unsupported RDFN and DFN models at K = 1.87

At K = 1.87 without support, the DFN had the larger maximum displacement at each displayed cycle, reversing the ordering at cycle 40,000 for K = 1.0 (Figs. 9(a,b) and 10(a,b)). At cycle 5,000, the displacement patterns extended laterally from the opening into both sidewalls. By cycle 40,000, the largest displacements in both networks were concentrated immediately around the opening, with lower values in the surrounding rock.

The supported models also showed a laterally elongated displacement pattern at cycle 5,000 (Fig. 10(c,d)). At cycle 40,000, the largest displacements were concentrated near the edge of the remaining opening and were offset towards its right side in both networks. The displacement zones around these concentrations differed in shape, even though the two maxima differed by only about 0.35%.

The fields indicate the location and shape of the main displacement concentrations within each panel. A quantitative comparison of their spatial extent would require a common displacement threshold because the panels use different colour scales. The snapshots describe the response through cycle 40,000. Section 4 describes crack patterns and cumulative bond breakage.

4 Damage evolution under different lateral stress conditions

4.1 Crack evolution and spatial distribution

Crack propagation and spatial distributions in the supported and unsupported RDFN and DFN models were compared to investigate the effects of the lateral pressure coefficient, joint morphology and rockbolt support on damage evolution.

Figure 11 shows crack development in the four cases at $K = 1.0$.

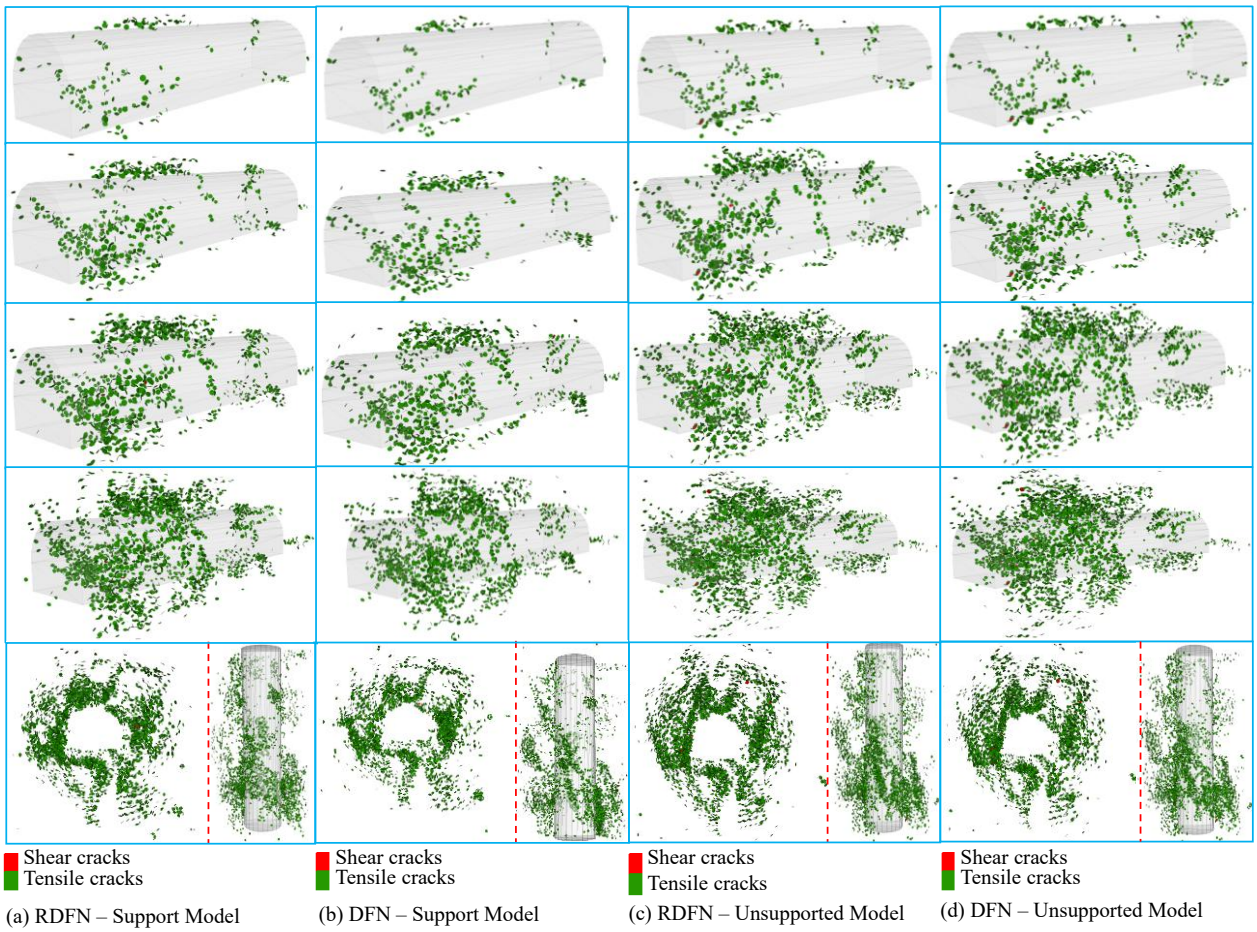


Fig. 11 Crack evolution in supported and unsupported models at $K = 1.0$

Cracks initially nucleated near joints and the excavation boundary, predominantly in tension with some localised shear cracking (Fig. 11). The crack count increased as the calculation proceeded, with multiple discontinuities influencing crack propagation and clustering toward the roof, floor and sidewalls. The resulting crack pattern was discontinuous and largely aligned with prominent discontinuities. The unsupported RDFN and DFN showed broadly similar crack distributions, with differences in the locations of local clusters. The displayed supported cases showed fewer cracks

around the opening and less extensive crack zones in the surrounding rock. Local differences nevertheless remained evident: cracks clustered strongly near the excavation surface, with subtle differences in coalescence, whereas farther from the surface the degree of clustering differed markedly between the left and right sidewalls. Joint morphology thus had a relatively pronounced influence on local crack evolution under supported conditions.

Crack-orientation distributions were analysed to further investigate the directional patterns (Fig. 12).

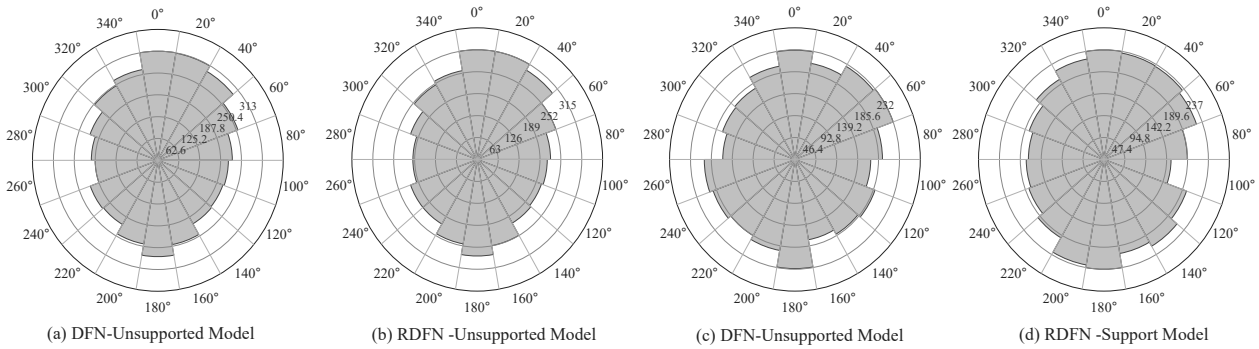


Fig. 12 Crack orientation distributions in the RDFN and DFN models at $K = 1.0$

At $K = 1.0$ without support, peak crack counts in the dominant orientation range were 315 for the DFN and 313 for the RDFN (Fig. 12(a,b)). The corresponding peaks in the supported cases were 237 and 232 (Fig. 12(c,d)). The differences relative to the unsupported cases were 24.8% for the DFN and 25.9% for the RDFN. The principal orientations were similar across the displayed cases, with differences in the detailed orientation distributions of the supported models.

Figure 13 shows crack development in the four cases at $K = 1.87$.

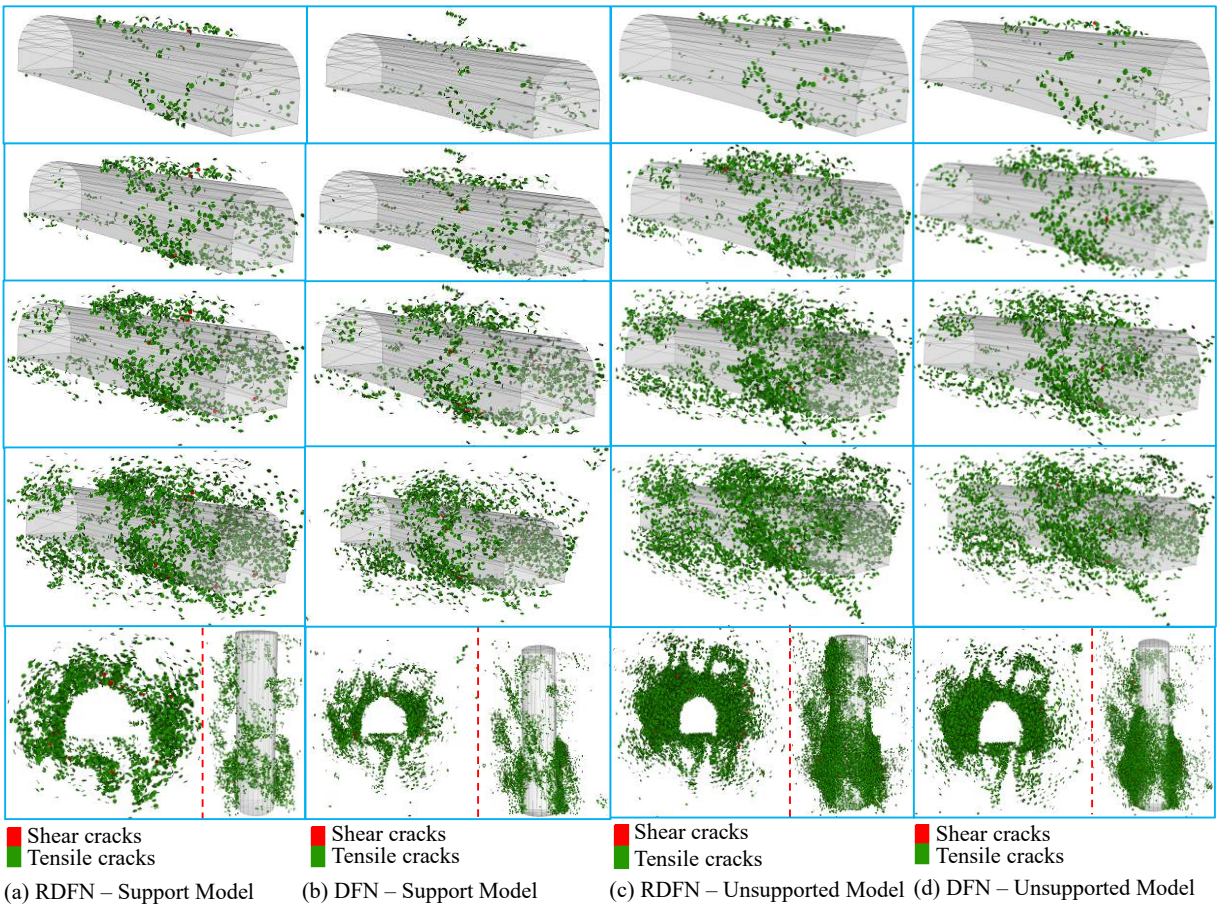
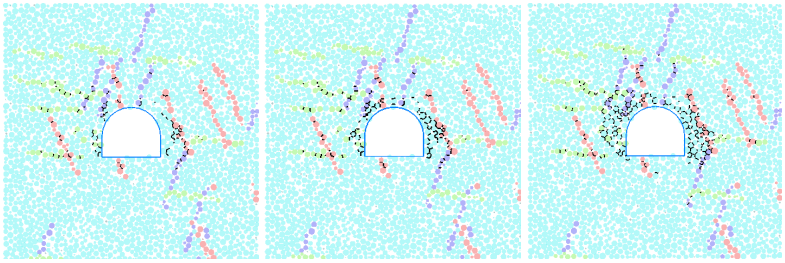


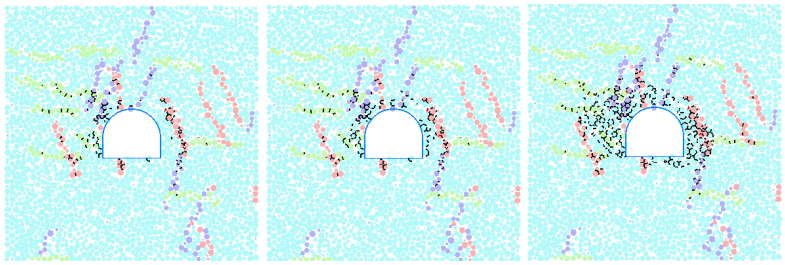
Fig. 13 Crack evolution in supported and unsupported models at $K = 1.87$

The initial crack locations differed between the two models (Fig. 13). Cracks subsequently propagated and formed broadly comparable clusters with different overall geometries. Without support, cracks extended from the excavation boundary into the deeper roof, floor and sidewalls, and local clusters progressively coalesced. Crack clustering was more pronounced in the unsupported RDFN. In the displayed supported cases, dense crack zones were smaller and less connected, with cracks concentrated closer to the opening.

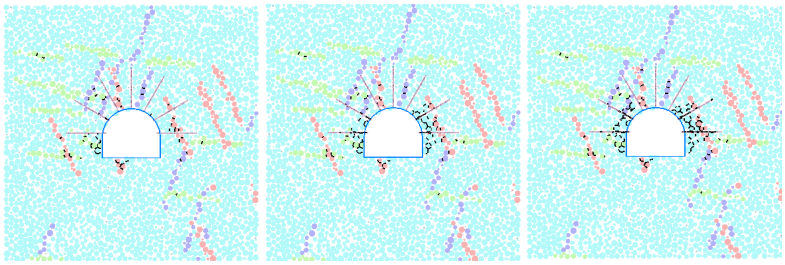
The section at $Y = 0.625$ m, corresponding to the first bolt row, was selected to examine crack propagation around the roadway (Fig. 14).



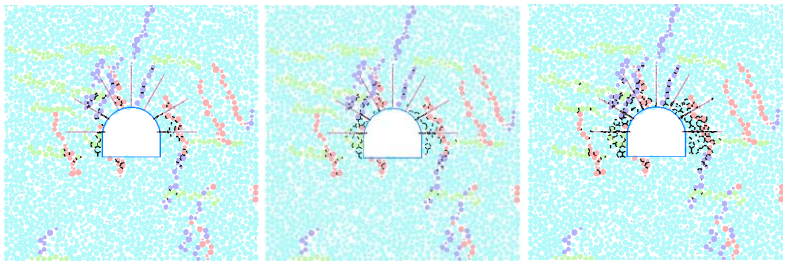
(a) Unsupported-DFN



(b) Unsupported-RDFN



(c) Supported-DFN



(d) Supported-RDFN

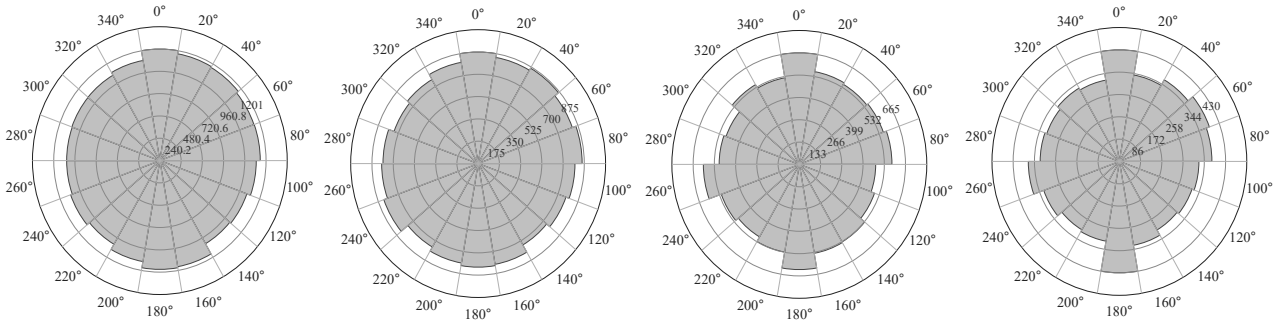
382

383 **Fig. 14** Crack evolution in the roadway cross-section at $Y = 0.625$ m

384 Without support, cracks first formed at joints around the opening and in adjacent regions, then
385 extended towards the roof, floor and sidewalls (Fig. 14(a,b)). Crack density was higher at the left
386 sidewall than at the right. This asymmetry is consistent with the nonuniform fracture arrangement,
387 although the contribution of individual fractures was not isolated. Distinct RDFN crack clusters
388 developed near the left sidewall and floor. With continued calculation, floor cracks tended to coalesce
389 with clusters at the base of the left sidewall, whereas this tendency was less evident in the DFN. In
390 the earlier outputs for the supported models (Fig. 14(c,d)), crack clusters were less pronounced.
391 Cracks subsequently appeared near bolt-particle connections, with dense tensile cracking near the

embedded ends of horizontal and shoulder bolts but fewer events around roof bolts. This spatial association suggests that anchorage altered local load transfer at the sidewalls and shoulders. Crack clustering nevertheless remained weaker than in the corresponding unsupported models. Proximity to a bolt does not by itself identify an event as failure of the bolt body, an interface or the surrounding rock.

Fig. 15 shows the crack orientation distributions at $K = 1.87$.



(a) RDFN -Unsupported Model (b) DFN-Unsupported Model (c) RDFN -Support Model (d) DFN -Support Model

Fig. 15 Crack orientation distributions in the RDFN and DFN models at $K = 1.87$

Without support, crack clusters occupied similar orientation ranges in the two models, and substantial cracking occurred in all directions (Fig. 15). Peak counts in the dominant orientations were 1,201 for the RDFN and 875 for the DFN. The corresponding peaks in the supported cases were 665 and 430, or approximately 44.6% and 50.9% below the respective unsupported counts. These differences refer to the dominant orientation bins.

4.2 Differences in crack count and support effectiveness

The PFC crack count is the cumulative number of recorded bond-breakage events. Figure 16 presents the reported totals for each fracture network and support condition at the two initial lateral pressure coefficients.

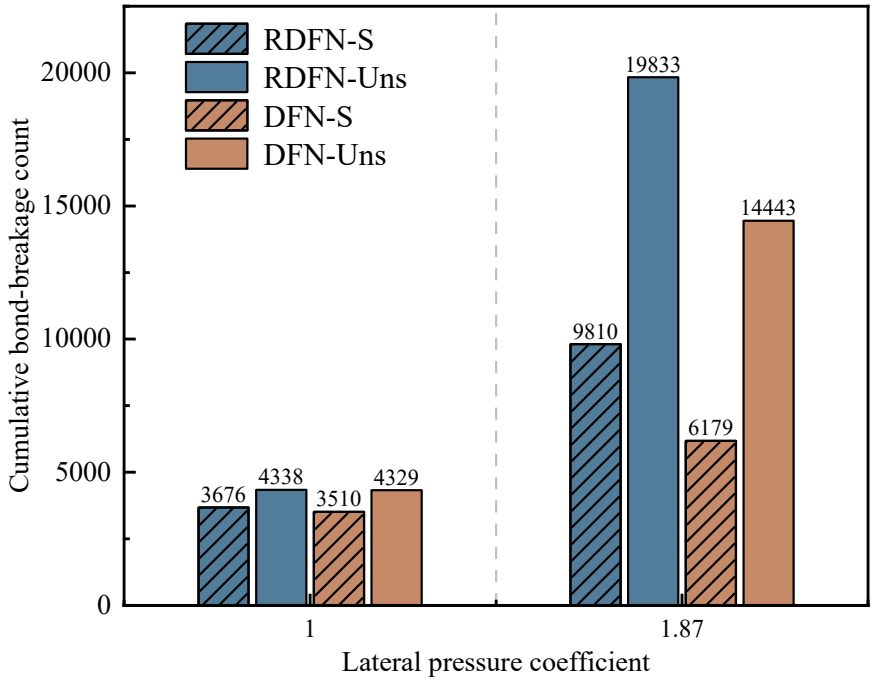


Fig. 16 Reported cumulative bond-breakage counts by initial lateral pressure coefficient, fracture network and support condition

The reported totals describe the recorded outcomes for the eight cases. Comparisons of crack accumulation over an equal calculation interval require counts from matching cycles.

The relative difference in crack count, R_c, was defined to quantify the difference between the RDFN and DFN under identical lateral stress and support conditions:

$$R_c = \frac{N_{RDFN} - N_{DFN}}{N_{DFN}} \times 100\% \tag{3}$$

where N_{RDFN} and N_{DFN} are the reported cumulative counts for the RDFN and DFN under the same initial lateral pressure coefficient and support condition. The DFN count is the denominator in Eq. (3).

Equation (4) expresses the difference between the reported unsupported and supported counts, E_c, as a percentage of the unsupported count for the same fracture network and initial lateral pressure coefficient.

$$E_c = \frac{N_{UnS} - N_S}{N_{UnS}} \times 100\% \tag{4}$$

where N_{UnS} and N_S denote the reported cumulative counts for the unsupported and supported cases, respectively.

At K = 1.0, the reported counts were 4,338 and 3,676 for the unsupported and supported RDFN, and 4,329 and 3,510 for the corresponding DFN cases. At K = 1.87, the reported counts were 19,833 and 9,810 for the RDFN, and 14,443 and 6,179 for the DFN, respectively.

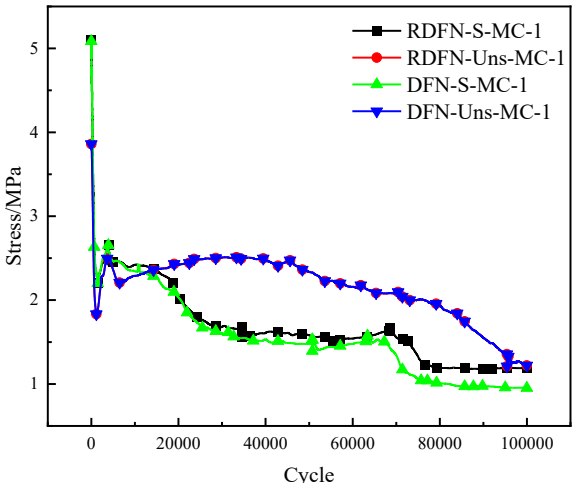
At K = 1.0, R_c was 0.21% for the unsupported cases and 4.73% for the supported cases. At K = 1.87, the corresponding values were 37.32% and 58.76%. For K = 1.87, the absolute RDFN–DFN difference was 5,390 events without support and 3,631 events with support. The supported cases had the greater relative difference because the DFN count, the denominator of R_c, was proportionally smaller.

Relative to the reported unsupported counts, the reported supported counts for the RDFN and DFN were 15.26% and 18.92% lower at K = 1.0, and 50.54% and 57.22% lower at K = 1.87, respectively.The reported bond-breakage counts provide a damage indicator alongside the displacement fields in Section 3.2.

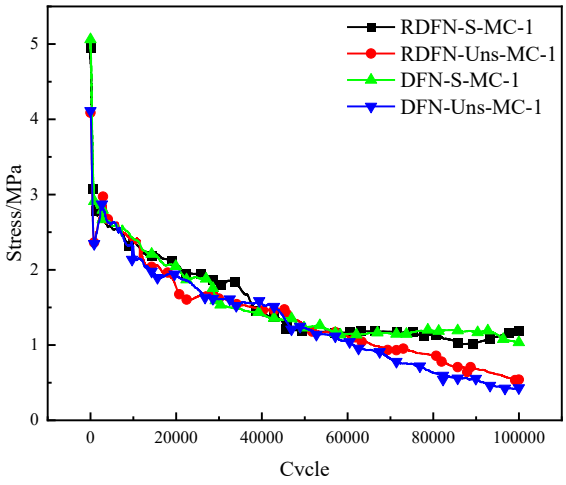
5 Stress redistribution and rockbolt load response

5.1 Evolution of surrounding rock stress

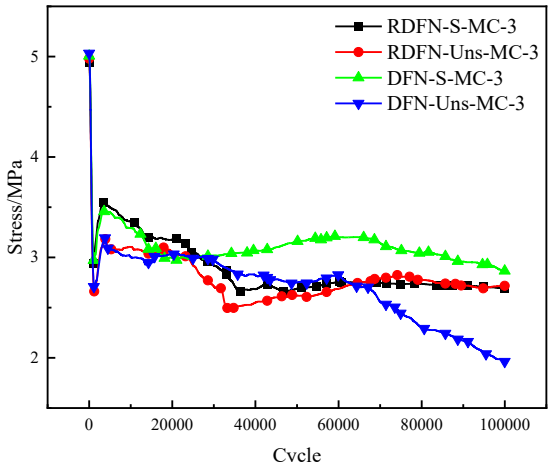
Stress redistribution around the roadway was examined at the roof arch (measurement circle 1), the left sidewall (circle 3) and the right sidewall (circle 4). Figure 17 shows these positions in panels (a,c,e) for K = 1.0 and panels (b,d,f) for K = 1.87, respectively. The RDFN and DFN were compared at each position under supported and unsupported conditions.



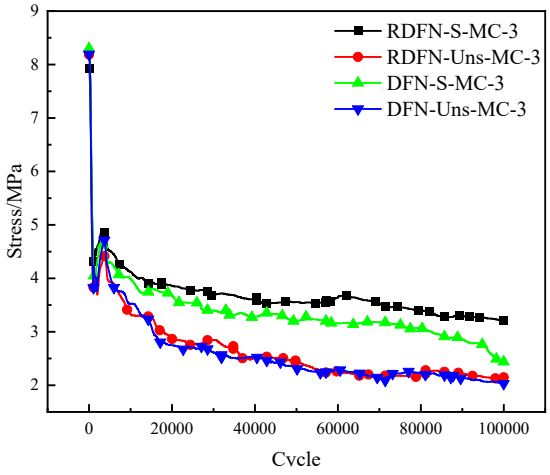
(a) Roof arch at K=1.0



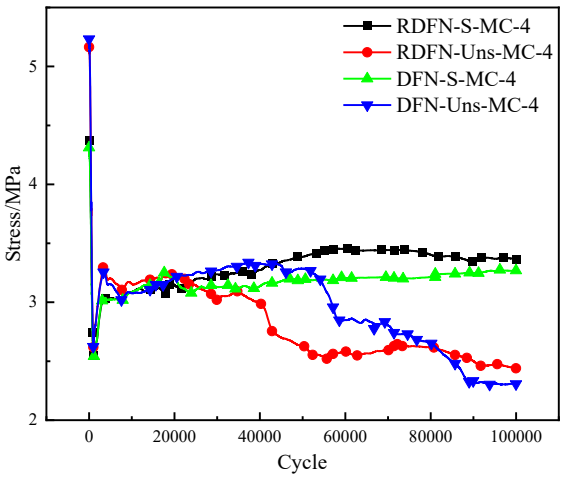
(b) Roof arch at K=1.87



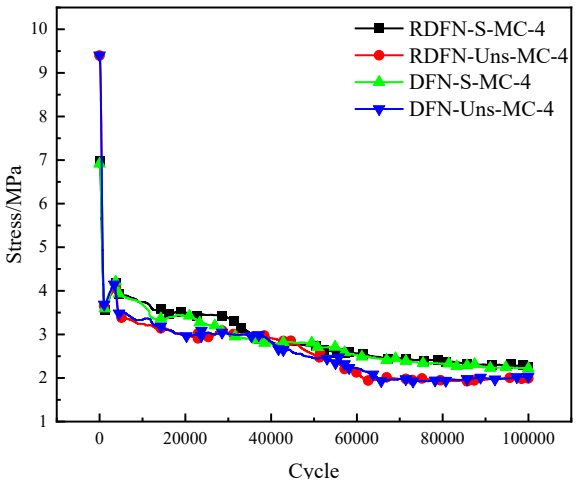
(c) left sidewall at K = 1.0



(d) left sidewall at K = 1.87



(e) right sidewall at K = 1.0



(f) right sidewall at K = 1.87

Fig. 17 Stress evolution around the roadway under different lateral stress conditions (S denotes supported models, Uns denotes unsupported models and MC denotes measurement circle)

At K = 1.0 (Fig. 17(a)), the roof-arch stress histories generally exhibited a rapid initial decrease, a brief recovery and subsequent adjustment. Stress continued to decrease in both supported models during the later stages, with final values of approximately 1.19 MPa in the RDFN and 0.95 MPa in the DFN. The two unsupported histories were nearly identical and both ended at approximately 1.22 MPa. Rockbolting therefore did not maintain a higher roof stress than the unsupported condition throughout the calculation. The reduction in roof stress reflects excavation-induced unloading and adjustments in load transfer.

Figs. 17(c) and 17(e) present the stress histories at the left and right sidewalls, respectively, for K = 1.0. At the left sidewall (Fig. 17(c)), the final monitored stresses in the supported and unsupported RDFN were similar, at approximately 2.69 and 2.72 MPa, respectively. In the DFN, however, the supported stress ended at approximately 2.87 MPa, compared with 1.96 MPa without support, indicating that the influence of rockbolting on left-sidewall stress evolution depended on joint morphology. At the right sidewall (Fig. 17(e)), the supported models exhibited partial stress recovery after initial unloading and subsequently retained higher stress levels, ending at approximately 3.36 MPa in the RDFN and 3.27 MPa in the DFN. The unsupported stresses continued to decrease during the later stages, reaching approximately 2.44 and 2.31 MPa, respectively. At K = 1.0, the right sidewall thus exhibited a more consistent response to support, whereas the left sidewall showed more pronounced differences between the two fracture-network models.

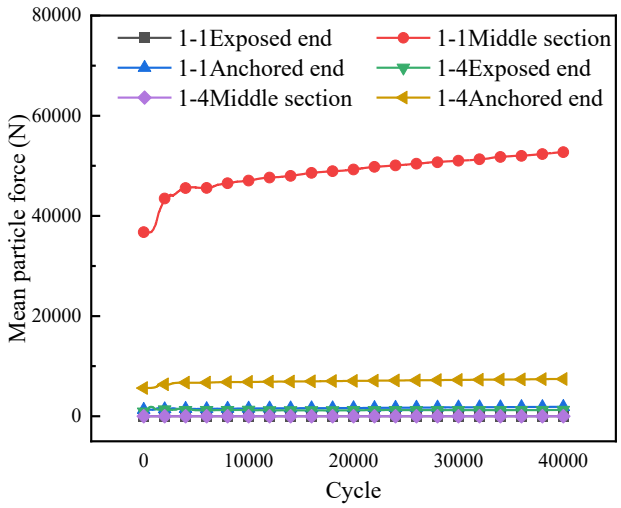
At K = 1.87, both supported models retained higher monitored stresses at all three locations by the end of the calculation (Fig. 17(b,d,f)). At the roof arch, the final values were 1.19 MPa in the supported RDFN and 1.03 MPa in the supported DFN, compared with 0.54 and 0.43 MPa in the unsupported cases. At the left sidewall, the corresponding values were 3.20 and 2.44 MPa with support and 2.15 and 2.03 MPa without support. The largest differences between supported and unsupported cases occurred at the left sidewall in the RDFN (1.05 MPa) and at the roof arch in the

DFN (0.60 MPa). At the right sidewall, both models showed smaller differences, with stresses of about 2.24 MPa with support and 2.00 MPa without support.

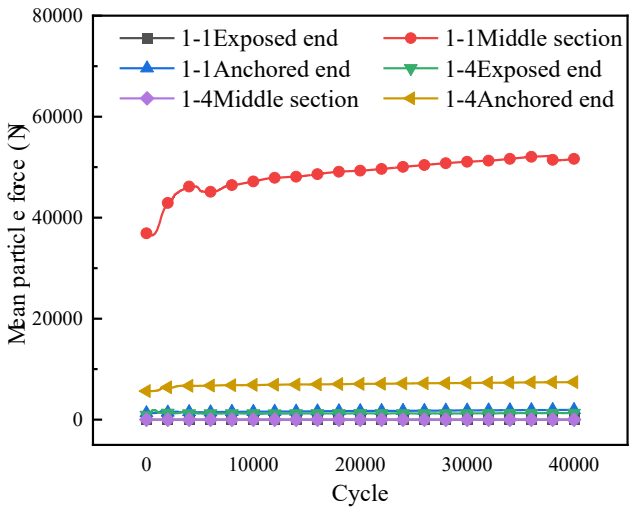
Comparing Fig. 17(c,d) and Fig. 17(e,f), increasing the lateral pressure coefficient raised the initial monitored sidewall stresses but did not increase the stress at every location after redistribution. For example, the supported right-sidewall stresses at the end of the calculation were lower at $K = 1.87$ than at $K = 1.0$, indicating that a higher initial stress does not necessarily result in greater local stress retention during the later stages. The influence of joint morphology was also spatially selective. At the supported left sidewall, the final DFN stress was slightly higher than the RDFN stress at $K = 1.0$ (Fig. 17(c)), whereas the RDFN stress was clearly higher at $K = 1.87$ (Fig. 17(d)). By contrast, the two right-sidewall histories remained close under the higher lateral stress condition (Fig. 17(f)). Changes in lateral stress therefore modified both the redistribution process and the spatial expression of differences between the two models.

5.2 Rockbolt force distribution and load transfer

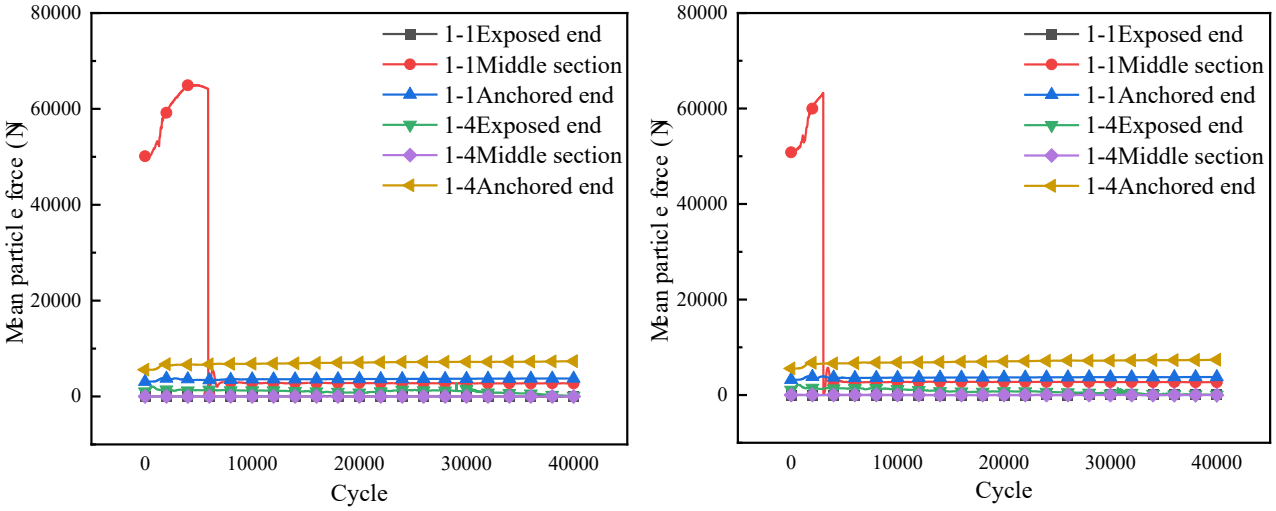
Figure 18 compares local mean particle force histories at the exposed end, middle segment and embedded end of two representative first-row rockbolts. Bolt 1-1 is the left horizontal bolt and bolt 1-4 is the vertical roof bolt. Panels (a,b) show the RDFN and DFN at $K = 1.0$, respectively, and panels (c,d) show the corresponding cases at $K = 1.87$.



(a) RDFN at K=1



(b) DFN at K=1



(c) RDFN at K=1.87 (d) DFN at K=1.87

Fig. 18 Forces in representative bolts of RDFN and DFN models under two lateral pressure coefficients

At K = 1.0 (Fig. 18(a,b)), the middle segment of horizontal bolt 1-1 had the highest local mean particle force among its three monitoring locations. It increased from 36.76 to 52.73 kN in the RDFN and from 36.90 to 51.64 kN in the DFN. The final values at its embedded end were 1.88 and 1.93 kN, respectively, and its exposed-end values were zero. For roof bolt 1-4, the largest values occurred at the embedded end, reaching 7.45 kN in the RDFN and 7.44 kN in the DFN at the end of the record. Its final exposed-end values were approximately 1.3 kN, while the middle-segment values remained close to zero.

At K = 1.87 (Fig. 18(c,d)), the local mean particle force at the middle segment of bolt 1-1 peaked at 65.01 kN in the RDFN and 63.28 kN in the DFN. Both curves dropped abruptly after the peak, with the drop occurring later in the RDFN. The final values were similar at 2.74 and 2.69 kN, respectively. The clearest difference between the two cases was therefore the timing of the post-peak drop. At K = 1.0, the same location showed an overall increase through the end of the record.

At the embedded end of horizontal bolt 1-1, the final local mean particle force was approximately 3.76 kN at K = 1.87, compared with about 1.9 kN at K = 1.0. At the embedded end of roof bolt 1-4, the final values at K = 1.87 were 7.36 and 7.39 kN in the RDFN and DFN, respectively, close to the values at K = 1.0. Thus, the strongest change across the two stress conditions occurred at

the middle segment of bolt 1-1, while the embedded end of bolt 1-4 showed a similar response in both conditions.

The particle-force histories show that the response to lateral stress varied along the two monitored bolts. The post-peak drop at bolt 1-1 suggests a change in local load transfer. Establishing the mechanism would require corresponding contact-slip or bond-failure histories and a separate estimate of the axial resultant across the bolt section.

6 Comparison with field observations

Numerical results under supported and unsupported conditions were compared with representative field failure patterns to evaluate the ability of the models to reproduce roadway deformation and failure (Fig. 19).

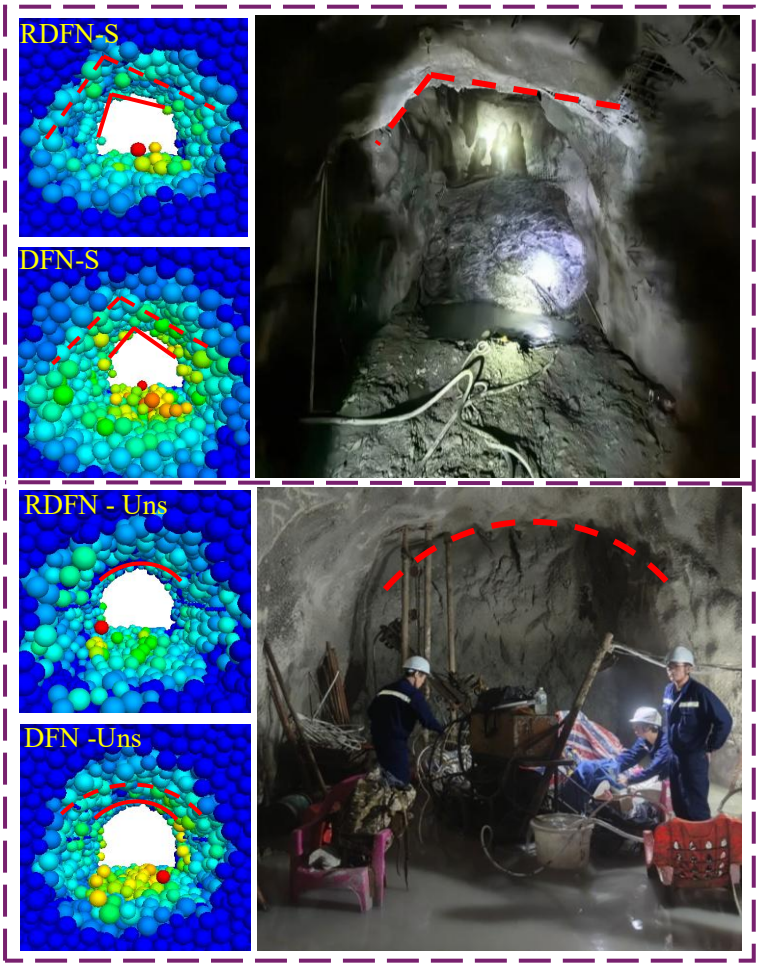


Fig. 19 Comparison of numerical and field roadway deformation and failure (Note:S: supported; Uns unsupported)

With support, deformation in both numerical models was concentrated at the roof arch and sidewalls, with localised roof deformation and sidewall convergence. The supported field roadway exhibited the same principal features while retaining a largely intact cross-section. Agreement in the main deformation locations and overall geometry suggests that rockbolting restricted the affected region, although local deformation remained concentrated at the roof arch and sidewalls.

Without support, high-displacement zones expanded in both models, roof and sidewall deformation increased markedly, and localised failure became more concentrated. The field roadway exhibited roof block falls, localised collapse and sidewall fragmentation over a larger area than the supported roadway. The numerical models therefore reproduced the principal unsupported response: a larger failure zone and more severe roof and sidewall damage.

The RDFN and DFN reproduced similar principal deformation locations but differed in the extent and continuity of localised high-displacement zones. Field photographs support qualitative agreement in roof damage, sidewall deformation and the overall contrast between supported and unsupported roadways. They do not validate model-scale displacement magnitudes, bolt forces or the complete imposed loading path. A field monitoring series matched to the model cases and output stages was not used, so quantitative prediction errors were not evaluated.

7 Discussion

Joint roughness contributes to shear resistance through geometric interlocking, and rough fracture networks have exhibited higher peak strength than planar networks under direct shear (Wang et al. 2020). Here, the unsupported RDFN exhibited greater maximum displacement at lower lateral stress but smaller displacement at higher lateral stress. Direct shear strength and excavation-induced displacement describe different responses under different loading and boundary conditions. The observed reversal may reflect competition between restraint of joint sliding and localised fracture development around asperities and rock bridges. Increased microcrack accumulation under higher normal stress and roughness provides a plausible basis for this interpretation (Meng et al. 2022).

However, direct evidence from joint slip and contact-force histories is required to distinguish these mechanisms. Planar-joint idealisation therefore cannot be assumed to provide consistently conservative deformation estimates.

At K = 1.87, the maximum displacements of the supported models differed by approximately 0.35% at cycle 40,000. The reported cumulative bond-breakage counts were 9,810 for the supported RDFN and 6,179 for the supported DFN. Displacement describes the magnitude of deformation, while cumulative bond breakage records damage in the particle assembly. Microcrack accumulation has been examined alongside energy dissipation during jointed-rock shear failure (Tai et al. 2023). Bonded-particle simulations also show that confinement changes how tensile force chains evolve during crack development (Zhang et al. 2025). PFC simulations of thermally damaged granite and sandstone linked macroscopic failure to both microcrack evolution and changes in effective mineral contacts. Although the loading conditions differ from roadway excavation, these simulations illustrate how contact-scale information can complement crack statistics when interpreting macroscopic behaviour (Du et al. 2026). These studies motivate interpreting bond-breakage counts alongside other indicators of internal damage and load transfer. Matching displacement and bond-breakage outputs by calculation cycle and distinguishing failures in the rock from failures associated with the support would clarify how damage and deformation evolve together.

Rockbolt reinforcement depends on load transfer between the bolts and the surrounding fractured rock. Anchorage and the bearing-instability response of broken rock provide a framework for interpreting this interaction (Li et al. 2022). In a fault-crossing roadway, combined grouting and reinforcement reduced deformation and roof separation, with field monitoring providing evidence of support performance (Li et al. 2024). For large-span caverns in fractured rock under low in-situ stress, field monitoring also documented deformation control after installation of a combined system of mortar bolts, prestressed anchor cables and steel arch ribs (Huang et al. 2026). The reported cumulative bond-breakage counts for the supported cases were lower than those for the corresponding

568 unsupported cases. At K = 1.87, the supported models also retained higher stresses at the roof arch
569 and both sidewalls at the end of the stress record. FDEM simulations of layered-rock tunnels showed
570 that increasing the density of prestressed constant-resistance cables produced diminishing
571 improvements in convergence control beyond an effective support range, while excessive support
572 increased cohesive-element failures. Although this support system differs from the bonded-particle
573 bolts considered here, the findings reinforce the need to evaluate support performance using both
574 deformation control and fracture development (Zhan et al. 2026). The local mean particle force
575 peaked at different positions along horizontal bolt 1-1 and roof bolt 1-4. The earlier post-peak drop
576 in the DFN at K = 1.87 suggests a difference in the timing of local load transfer between the two
577 network models. Relating this change to bolt or interface failure requires contact-scale evidence and
578 the axial force resultant across the bolt section.

579 The findings remain conditional on the adopted network, roughness and loading conditions.
580 Geometric similarity between DFNs does not guarantee mechanical equivalence (Yin and Chen 2020),
581 and multiple network realisations provide a means of examining the associated uncertainty (Sarmast
582 Sakhvidi et al. 2026). The present paired-network comparison does not establish variability across
583 fracture arrangements. Changing horizontal stress at fixed vertical stress also changes both the stress
584 ratio and loading magnitude, so their separate contributions cannot be identified from these two cases.
585 The displacement and force values are model-scale responses under a protocol in which Z-direction
586 servo control was deactivated after initialisation. Their transfer to constant far-field loading or field
587 excavation requires verification of the subsequent boundary constraints and of the scaling
588 relationships.

589 The trace-length offsets used in the network inputs are an additional source of geometric
590 uncertainty. Their physical interpretation and sensitivity were not assessed independently, and the
591 fitted field distributions do not fully specify the sampling settings used for this single network.
592 Broader assessment should document the complete fracture-sampling and particle-discretisation

593 settings, test the influence of the input processing, separate rock and support-related bond-breakage
594 events, and compare response measures at common cycles. Quantitative field measurements and
595 independent interface calibration would also strengthen transfer to engineering design.
596 Photogrammetric characterisation can support spatially informed hazard assessment, as demonstrated
597 for unstable red-bed rock masses, but the present approach requires further site-specific validation
598 before application to other excavations or rock-slope settings.

599 **8 Conclusions**

600 Controlled comparisons of rough and planar fracture networks under the investigated numerical
601 conditions yielded the following conclusions:

602 (1) The effect of joint roughness on roadway deformation depends on lateral stress. Increasing
603 lateral stress reversed the ordering of the maximum displacements of the unsupported models, with
604 the planar-joint model exhibiting greater sensitivity of deformation to lateral stress. Planar-joint
605 idealisation therefore does not introduce a consistently conservative bias.

606 (2) At both lateral pressure coefficients, the reported cumulative bond-breakage counts were
607 higher for the RDFN than for the corresponding DFN and lower for the supported cases within each
608 network.

609 (3) Rockbolting narrowed the difference in maximum displacement between the networks. At K
610 = 1.87, both supported models retained higher stresses at the roof arch and both sidewalls at the end
611 of the calculation. The largest support-related stress difference was at the left sidewall in the RDFN
612 and at the roof arch in the DFN.

613 (4) For the two representative first-row bolts, the highest local mean particle forces occurred at
614 the middle segment of horizontal bolt 1-1 and the embedded end of roof bolt 1-4. At K = 1.87, the
615 middle-segment force of bolt 1-1 dropped abruptly after the peak, later in the RDFN than in the DFN.
616 This difference concerns the timing of the local particle-force response.

617 **Acknowledgements**

This work was financially supported by the National Natural Science Foundation of China (No. 52574101), the specific research fund of the Innovation Platform for Academicians of Hainan Province (YSPTZX202504), and the Hainan Province Science and Technology Special Fund (ZDYF2024GXJS307).

Author contributions

Haoyu Sun developed the numerical models, performed the formal analysis and validation, prepared the visualisations, and wrote the original draft. Peitao Wang conceived the study, contributed to the methodology, supervised the research, reviewed and edited the manuscript, and secured funding. Qi Gou contributed to the methodology and investigation and curated the data. Yi Chai and Long Tao participated in the investigation and provided research resources.

Declaration of competing interest

The authors declare no competing interests.

Data availability statement

The datasets generated and analysed during the current study are available from the corresponding author upon reasonable request.

References

Bandis S, Lumsden AC, Barton NR (1981) Experimental studies of scale effects on the shear behaviour of rock joints. Int J Rock Mech Min Sci Geomech Abstr 18:1–21. https://doi.org/10.1016/0148-9062(81)90262-X

Barton N (1973) Review of a new shear-strength criterion for rock joints. Eng Geol 7:287–332. https://doi.org/10.1016/0013-7952(73)90013-6

Bonnet E, Bour O, Odling NE, Davy P, Main I, Cowie P, Berkowitz B (2001) Scaling of fracture systems in geological media. Rev Geophys 39:347–383. https://doi.org/10.1029/1999RG000074

641 Cai MF, Xue DL, Ren FH (2019) Current status and development strategy of metal mines. Chin J
642 Eng 41:417–426. https://doi.org/10.13374/j.issn2095-9389.2019.04.001
643 Chen M, Yang SQ, Ranjith PG, Zhang YC (2020) Cracking behavior of rock containing non-
644 persistent joints with various joints inclinations. Theor Appl Fract Mech 109:102701.
645 https://doi.org/10.1016/j.tafmec.2020.102701
646 Chen X, Sun JY, Yang P, Feng ZL, Xie TG, Chen KX (2017) Influence of joint spacing and
647 inclination angle on fragmentation characteristic of rock masses under uniaxial compression. J
648 Min Saf Eng 34:608–614. https://doi.org/10.13545/j.cnki.jmse.2017.03.029
649 Cho N, Martin CD, Sego DC (2007) A clumped particle model for rock. Int J Rock Mech Min Sci
650 44:997–1010. https://doi.org/10.1016/j.ijrmms.2007.02.002
651 Cui W, Wang LX, Luo YJ (2022) Modeling of three-dimensional single rough rock fissures: a study
652 on flow rate and fractal parameters using the Weierstrass-Mandelbrot function. Comput Geotech
653 144:104655. https://doi.org/10.1016/j.compgeo.2022.104655
654 Du X, Chen YL, Pan YG, Lu B, Jia P, Fernandez-Steeger TM, Azzam R (2026) Microscopic damage
655 evolution and failure mechanisms of rocks with different mineral compositions under thermal-
656 mechanical loading. Rock Mech Bull. https://doi.org/10.1016/j.rockmb.2026.100372
657 Fan X, Yang ZJ, Li KH (2021) Effects of the lining structure on mechanical and fracturing behaviors
658 of four-arc shaped tunnels in a jointed rock mass under uniaxial compression. Theor Appl Fract
659 Mech 112:102887. https://doi.org/10.1016/j.tafmec.2020.102887
660 Gou Q, Wang PT, Jing GY, Cai MF (2024) Influence of 3D joint roughness on fracture behaviours
661 of rock mass subjected to compression. Geomat Nat Hazards Risk 15:2385626.
662 https://doi.org/10.1080/19475705.2024.2385626
663 Houben G, Weitkamp A, Kaufhold S (2024) The roughness of fracture surfaces and its scale
664 dependence – a methodological study based on natural fractures in sandstones from Southern
665 Germany. Environ Earth Sci 83:388. https://doi.org/10.1007/s12665-024-11699-8

666 Hu M, Liu R, Li S, Yuan C, Feng X (2026) Numerical study on instability of rock structural planes
667 induced by stress disturbances. Environ Earth Sci 85:355 https://doi.org/10.1007/s12665-026-
668 13094-x
669 Huang N, Liu RC, Jiang YJ, Cheng YF (2021) Development and application of three-dimensional
670 discrete fracture network modeling approach for fluid flow in fractured rock masses. J Nat Gas
671 Sci Eng 91:103957. https://doi.org/10.1016/j.jngse.2021.103957
672 Huang X, Yu Z, Tian M, Lin R, Li Q, Shi C (2026) Stability control and support optimization for
673 large-span underground caverns in fractured rock masses under low in-situ stress. Environ Earth
674 Sci 85:389. https://doi.org/10.1007/s12665-026-13124-8
675 Komvopoulos K, Ye N (2001) Three-dimensional contact analysis of elastic-plastic layered media
676 with fractal surface topographies. J Tribol 123:632–640. https://doi.org/10.1115/1.1327583
677 Kulatilake PHSW, Balasingam P, Park J, Morgan R (2006) Natural rock joint roughness
678 quantification through fractal techniques. Geotech Geol Eng 24:1181–1202.
679 https://doi.org/10.1007/s10706-005-1219-6
680 Li HB, Pan WP, Hua XZ, Luan B, Huang ZJ (2024) Instability characteristics of surrounding rock
681 and surrounding rock control technology of deep coal roadway crossing the fault: a case study
682 of Zhuxianzhuang coal mine. Geomat Nat Hazards Risk 15:2366376.
683 https://doi.org/10.1080/19475705.2024.2366376
684 Li JZ, Gao FQ, Lou JF, Yuan GY (2022) Study on reinforcement and bearing-instability mechanism
685 of broken rock mass. J Min Saf Eng 39:1125–1134.
686 https://doi.org/10.13545/j.cnki.jmse.2021.0583
687 Li M, Deng H, Tu GX (2024) A study of rock mass properties based on discrete fracture network
688 modeling and compression damage process. Bull Eng Geol Environ 83:402.
689 https://doi.org/10.1007/s10064-024-03898-1

690 Li WT, Li SC, Xuan C, Wang Q, Wang X, Shao X (2015) Mechanism and control of failure of rock
691 roadway support in highly stressed soft rock. Chin J Rock Mech Eng 34:1836–1848.
692 https://doi.org/10.13722/j.cnki.jrme.2014.1594
693 Liu DP, Liu JC, Xu Y, Cao ZK, Xia KW (2026) Energy evolution and failure characteristics of shale
694 under true-triaxial unloading paths. Bull Eng Geol Environ 85:641.
695 https://doi.org/10.1007/s10064-026-05279-2
696 Meng FZ, Song J, Yue ZF, Zhou H, Wang XS, Wang ZQ (2022) Failure mechanisms and damage
697 evolution of hard rock joints under high stress: insights from PFC2D modeling. Eng Anal Bound
698 Elem 135:394–411. https://doi.org/10.1016/j.enganabound.2021.12.007
699 Sarmast Sakhvidi M, Khosravi MH, Havaej M, Kargar AR (2026) Stability assessment of tunnel
700 portal using DFN-DEM modeling and photogrammetry: a case study of Tehran-Shomal freeway
701 in Iran. Eng Geol 372:108981. https://doi.org/10.1016/j.enggeo.2026.108981
702 Shang C, Li L, Chu K, Zhou Z, Casas G, Tu W, Chen Y, Sun S (2024) A coarse-grained bonded
703 particle model for large-scale rock simulation. Rock Mech Bull 3:100133.
704 https://doi.org/10.1016/j.rockmb.2024.100133
705 Tai DP, Qi SW, Zheng BW, Wang CL, Guo SF, Luo GM (2023) Shear mechanical properties and
706 energy evolution of rock-like samples containing multiple combinations of non-persistent joints.
707 J Rock Mech Geotech Eng. 15:1651–1670 https://doi.org/10.1016/j.jrmge.2022.11.014
708 Tang QH, Zhang CL, Zhang GW, Jiao ZL (2021) Quantization algorithm of joint roughness
709 coefficient based on standard joint roughness curves. Chin J Rock Mech Eng 40:1402–1411.
710 https://doi.org/10.13722/j.cnki.jrme.2020.0960
711 Tatone BSA, Grasselli G (2010) A new 2D discontinuity roughness parameter and its correlation with
712 JRC. Int J Rock Mech Min Sci 47:1391–1400. https://doi.org/10.1016/j.ijrmms.2010.06.006

Wang D, Dong J, Liu D, Chen X, Zhong H, Yang M, Wang H (2026) Investigation of shale fracture behavior with different bedding properties based on discrete element method. Rock Mech Bull. 5:100243 https://doi.org/10.1016/j.rockmb.2025.100243

Wang PT, Yang TH, Xu T, Cai MF, Li CH (2016) Numerical analysis on scale effect of elasticity, strength and failure patterns of jointed rock masses. Geosci J 20:539–549. https://doi.org/10.1007/s12303-015-0070-x

Wang PT, Ren FH, Tan WH, Yan ZX, Cai MF, Yang TH (2017) Development and mechanical behavior of a rough discrete joint network model under uniaxial compression. Rock Soil Mech 38(S1):70–78. https://doi.org/10.16285/j.rsm.2017.S1.008

Wang PT, Ren FH, Cai MF (2018) Mechanical analysis and size effect of rough discrete fractures network model under direct shear tests based on particle flow code. J China Coal Soc 43:976–983. https://doi.org/10.13225/j.cnki.jccs.2017.1061

Wang PT, Ren FH, Cai MF (2020) Influence of joint geometry and roughness on the multiscale shear behaviour of fractured rock mass using particle flow code. Arab J Geosci 13:165. https://doi.org/10.1007/s12517-020-5187-1

Wang PT, Ma C, Liu C, Liu QR, Fu YL, Cai MF (2023a) Anisotropic behavior of excavated layered rock mass subjected to compression considering the joint roughness. Bull Eng Geol Environ 82:373. https://doi.org/10.1007/s10064-023-03400-3

Wang PT, Ma C, Zhang B, Gou Q, Tan WH, Cai MF (2023b) Development of an improved three-dimensional rough discrete fracture network model: method and application. Int J Min Sci Technol 33:1469–1485. https://doi.org/10.1016/j.ijmst.2023.10.004

Xue B, Liu H, Wan B, Ren Y, Jing H (2026) Effects of joint roughness and inclination on fracture behavior of jointed rock under true triaxial compression. Environ Earth Sci 85:153. https://doi.org/10.1007/s12665-026-12816-5

737 Yang XX, Kulatilake PHSW (2019) Effect of joint micro mechanical parameters on a jointed rock
738 block behavior adjacent to an underground excavation: a particle flow approach. Geotech Geol
739 Eng 37:431–453. https://doi.org/10.1007/s10706-018-0621-9
740 Yang SQ, Yin PF, Zhang YC, Chen M, Zhou XP, Jing HW, Zhang QY (2019) Failure behavior and
741 crack evolution mechanism of a non-persistent jointed rock mass containing a circular hole. Int
742 J Rock Mech Min Sci 114:101–121. https://doi.org/10.1016/j.ijrmms.2018.12.017
743 Yin TC, Chen QF (2020) Simulation-based investigation on the accuracy of discrete fracture network
744 (DFN) representation. Comput Geotech 121:103487. https://doi.org/
745 10.1016/j.compgeo.2020.103487
746 Yuan W, Liu SF, Tan HH, Niu JD, Jiang ZL, Li XL, Peng S, Xue YY, Wang W, Sun XY (2021) A
747 new approach for quantifying the two-dimensional joint roughness coefficient (JRC) of rock
748 joints. Environ Earth Sci 80:484. https://doi.org/10.1007/s12665-021-09780-7
749 Zhan J, Tao Z, Ren S, Yang H, He M, Ming W (2026) Effect of anisotropic tunnel large-deformation
750 control based on a prestressed constant-resistance cable: Insights from 2D-finite-discrete
751 element and finite element method simulation. Rock Mech Bull 5:100273.
752 https://doi.org/10.1016/j.rockmb.2025.100273
753 Zhang B, Yang K, Yang Y (2026) Study on anchor cable and steel truss support for large deformation
754 in deep-buried layered soft rock tunnels. Bull Eng Geol Environ 85:409.
755 https://doi.org/10.1007/s10064-026-05078-9
756 Zhang M, Konietzky H, Song Z (2025) Evolution of force network, contact network, and tensile force
757 chains in rock-like bonded granular materials under unconfined and confined compression: A
758 DEM study. Environ Earth Sci 84:320. https://doi.org/10.1007/s12665-025-12288-z
759 Zhang SR, Qiu SL, Jiang Q, Kou YY, Zhang H, Xie ZK (2025) Deformation failure mechanism and
760 support effect in deep fractured rock masses. Bull Eng Geol Environ 84:593.
761 https://doi.org/10.1007/s10064-025-04627-y

762 Zheng Z, Yang B, Huang X, Zhang Q, Xia K, Li S, Cai W (2025) Shear cracking process and
763 micromechanism of intermittent joint: Insights from true triaxial shear test and PFC3D-GBM
764 simulation. Rock Mech Bull. https://doi.org/10.1016/j.rockmb.2025.100276
765